Understanding the Causes of Satellite–Model Discrepancies in Aerosol–Cloud Interactions Using Near-LES Simulations of Marine Boundary Layer Clouds

Shaoyue Qiu[1], Xue Zheng[1], Peng Wu[2], Hsiang-He Lee[1], and Xiaoli Zhou[3]

[1]Atmospheric, Earth, and Energy Division, Lawrence Livermore National Laboratory, Livermore, CA, U.S.A.
[2]Atmospheric, Climate, & Earth Sciences Division, Pacific Northwest National Laboratory, Richland, WA 99354, Washington, USA.
[3]Department of Physics and Atmospheric Science, Dalhousie University, Halifax, NS, Canada

Correspondence to: Xue Zheng (zheng7@llnl.gov)

Submitted to Atmospheric Chemistry and Physics 17 July 2025

Abstract. Aerosol–cloud interactions (ACI) remain the largest source of uncertainty in model estimates of anthropogenic radiative forcing, primarily because of deficiencies in representing aerosol–cloud microphysical processes that lead to inconsistent cloud liquid water path (LWP) responses to aerosol perturbations between observations and models. To investigate this discrepancy, we conducted a series of large-eddy scale simulations driven by realistic meteorology over the Eastern North Atlantic, and evaluated LWP susceptibility, precipitation processes, and boundary layer thermodynamics using satellite and ground-based observations.

Simulated LWP responses show a strong dependence on cloud state. Non-precipitating thin clouds exhibit a modest LWP decrease with increasing cloud droplet number concentration (N_d), consistent in sign but weaker in magnitude than satellite estimates, reflecting enhanced turbulent mixing and evaporation. The largest model-observation discrepancy occurs in non-precipitating thick clouds, where simulated LWP susceptibilities are strongly positive ($+0.32$) while observations indicate large negative values (-0.69). This discrepancy stems from excessive precipitation driven by underestimated entrainment, overly active accretion, and overly broad drop-size distributions in polluted conditions. While our high-resolution setup mitigates the excessive drizzling common in coarser models and captures key regime transitions, these biases persist—highlighting that improved parameterization of cloud-top processes, precipitation, and aerosol effects are needed beyond simply increasing model resolution.

Additionally, misrepresented moisture inversions in reanalysis introduce a moist bias in cloud-top relative humidity, further amplifying positive LWP susceptibility. Our results also suggest that large negative N_d–LWP relationships in observations may reflect internal cloud processes rather than true ACI effects.

1. Introduction

Marine boundary layer clouds exhibit substantial influence on Earth's radiation balance due to their high albedo and extensive global coverage. Aerosols modulate cloud albedo through changing cloud droplet number concentration (N_d), cloud liquid water path (LWP), and cloud fraction. The estimated radiative cooling from aerosols partially offset the warming from greenhouse gas emission (Slingo 1990). However, aerosol-cloud interaction (ACI) remains the most uncertain component of anthropogenic radiative forcing (Foster et al., 2021). In particular, liquid-phase cloud adjustments in LWP, cloud fraction, and cloud lifetime present the largest uncertainties in determining the net radiative forcing of ACIs, especially under varying large-scale conditions (Han et al., 2002; Small et al., 2009).

Among these uncertainties, the LWP response to aerosol perturbations has drawn particular attention due to its large spread in both observations and numerical model simulations. Theoretically, increasing aerosols would reduce droplet size and suppress precipitation, thereby increasing LWP and cloud lifetime (Albrecht, 1989). However, smaller droplets might also enhance evaporation and entrainment, leading to a reduced LWP in non-precipitating clouds (Ackerman et al., 2004; Xue and Feingold, 2006; Bretherton et al., 2007). This competition between processes leads to a bifurcated LWP response that varies with aerosol concentration, cloud type, and background meteorology.

In recent years, numerous satellite studies have reported an overall decrease of LWP with increasing N_d for non-precipitating clouds in polluted environments and an increase in LWP for precipitating clouds (e.g., Gryspeerdt et al. 2019, 2021; Toll et al., 2019; Zhang et al., 2022, 2023; Qiu et al., 2024; Yuan et al., 2023; 2025). In contrast, current global climate models (GCM) mostly simulate a positive LWP response to aerosol perturbation regardless the cloud conditions, which leads to an over-estimation of the aerosol-induced radiative forcing that is dominated by ACI (e.g., Ghan et al., 2016; Michibata et al., 2016; Mülmenstädt et al., 2024). This discrepancy could stem from the poorly resolved cloud processes in GCM due to its coarse horizontal resolution (~100 km). Recent development in computing have enable the global convection-permitting models (GCPMs) with kilometer-scale grid spacing, serving as an invaluable complement to the traditional climate models (e.g. Satoh et al., 2019; Stevens et al., 2019; Caldwell et al., 2021; Donahue et al., 2024). Notably, Sato et al. (2018) employed a GCPM and simulated a negative LWP response, attributing it primarily to better resolved evaporation and condensation processes from aerosol perturbations. Yet, other CPM studies with finer resolution than Sato et al. (2018) mostly simulate an increase in LWP with aerosol perturbations (e.g., Fons et al., 2024; Christensen et al, 2024), largely due to uncertainties in microphysics schemes, particularly regarding the treatment of precipitation (White et al., 2017).

Since most current GCPMs and GCMs adopt two-moment microphysics schemes, it is important to evaluate the precipitation parameterization in these schemes with observational constraints, in addition to the influence of precipitation process on the simulated ACI. Meanwhile, Terai et al. (2020) found that the lack of decrease in LWP in kilometer-scale models could be due to the lack of resolving the sub-kilometer processes that are most relevant to ACI processes. For example, they found that when increasing model resolution from 4 km to 250m, the fraction of precipitating clouds largely decreases, especially for thick clouds, and the LWP response becomes negative for non-precipitating clouds. Therefore, it is critical to assess the benefit of increasing model resolution to near large-eddy simulation (LES) scale in representing precipitation, as well as the evaporation-entrainment feedback responsible for LWP reduction without altering the structure of the microphysics parameterization and ultimately reconcile the LWP adjustment observed by satellite with those estimated by GCM and GCPM.

With model resolutions ranging from 25 m to 200 m, numerous LES studies have utilized idealized meteorological conditions and have provided valuable process-level understanding on the mechanisms governing cloud responses to aerosol perturbations (e.g., Xue and Feingold, 2006; Xue et al., 2008; Bretherton 2007; Seifert et al., 2015; Glassimire et al., 2019; Hoffman et al., 2020; Chen et al., 2024; Zhang et al., 2024). However, ACI and cloud processes using idealized simulations cannot be directly evaluated or constrained by observations, limiting their ability to explain the divergent LWP response between the two. Additionally, many LES studies are conducted with limited domain size, which cannot resolve mesoscale organization and variability of cloud and precipitation, both of which have been shown to significantly affect retrieved N_d-LWP relationships (e.g., Zhou and Feingold; 2023; Kokkola et al., 2025; Tian et al., 2025). Finally, both aerosol and cloud fields are strongly modulated by synoptic conditions (e.g., Engström and Ekman, 2010, Zheng et al. 2011, Zheng et al. 2025). LES studies focused on a small number of cases fail to capture the influence of cloud regimes and synoptic variabilities on ACI, both of which determine the magnitude and sign of cloud responses to aerosol perturbations.

The Eastern North Atlantic (ENA) region is uniquely suited to address this issue due to its location at the transition between midlatitude and subtropical regimes, experiencing various synoptic conditions and cloud regimes (e.g., Remillard & Tselioudis, 2015; Zheng et al., 2025). In addition, the ENA region and the availability of long-term, high-quality ground-based observations from the DOE Atmospheric Radiation Measurement (ARM) program make it possible for process-level evaluation with the comprehensive observations. Marine boundary layer (MBL) clouds in this region are frequently drizzling and sensitive to aerosol and meteorological perturbations, making them ideal for studying aerosol-cloud-precipitation interactions (Wood et al., 2015).

The goal of this study is to evaluate key ACI processes, such as precipitation suppression and evaporation-entrainment feedback, as well as precipitation treatment in a two-moment scheme, through simulations approaching LES scales. To address limitations in previous LES studies, we perform a series of simulations using a nested-domain configuration to seamlessly simulate the realistic circulations across different synoptic regimes, with the innermost domain spanning 1°×1°, consistent with typical GCM grid spacing and the spatial scale used in satellite observations to quantify N_d-LWP relationships (introduced in Sect. 2). To investigate the variation of ACI across different synoptic conditions, we simulated an ensemble of realistic MBL cloud cases across three synoptic regimes, each characterized by northerly surface flow over the ENA site. The classification of synoptic regimes is based on our previous study (Zheng et al., 2025), in which seven major synoptic regimes were identified using both surface and mid-level meteorological data. To enable a process-level evaluation of the parameterization of the warm rain process, we leverage ground-based radar measurement from the DOE ARM ENA site and apply a newly developed radar simulator for direct model-observation comparison.

2. Data and Methodology

2.1 Datasets

This study adopts both satellite and ground-based observations to assess the simulated cloud, precipitation processes, and ACI processes. For satellite observations, we used cloud retrievals derived from the Spinning Enhanced Visible InfraRed Imager (SEVIRI) on the geostationary satellite Meteosat-10 and Meteosat-11 over the ENA region. The cloud retrievals are based on the methods developed by the Clouds and the Earth's Radiant Energy System (CERES) project using the Satellite ClOud and Radiation Property retrieval System (SatCORPS) algorithms (Minnis et al., 2011, 2021; Painemal et al., 2021). The SEVIRI Meteosat cloud retrieval products are pixel-level cloud retrievals produced by NASA LaRC SatCORPS group, specifically tailored to support the ARM program over the ARM ground-based observation sites. For Meteosat-10 and Meteosat-11 cloud retrievals, they have a spatial resolution of 4-km and 3-km at nadir and an hourly and half-hourly temporal resolution, respectively.

In this study, we used the cloud mask, cloud effective radius (r_e), cloud optical depth (τ), LWP, cloud phase, and cloud top height variables in the SEVIRI Meteosat cloud retrieval product (Minnis et al., 2011, 2021). We focus on warm boundary layer clouds with cloud top below 3km and a liquid cloud phase. The r_e and τ retrievals are based on the shortwave-infrared split window technique during the daytime. Cloud LWP is derived from r_e and τ using the equation: $LWP = \frac{4 r_e \tau}{3 Q_{ext}}$, where Q_{ext} represents the extinction efficiency and assumed constant of 2.0. Cloud mask algorithm is consistent with the CERES Ed-4 algorithm, as described in Trepte et al. (2019), where cloudy and clear pixels are distinguished based on the calculated TOA clear-sky radiance. Cloud top height is derived from the retrieved cloud effective and top temperature, together with the boundary-layer temperature profiles and lapse rate, as described in Sun-Mack et al. (2014). Cloud N_d is retrieved based on the adiabatic assumptions for warm boundary layer clouds, based on the following equation:

$$N_d = \frac{\sqrt{5}}{2\pi k}\left(\frac{f_{ad} c_w \tau}{Q_{ext} \rho_w r_e^5}\right)^{1/2} \tag{1}$$

In Equation (1), k represents the ratio between the volume mean radius and r_e, and it is assumed to be constant of 0.8 for stratocumulus, f_{ad} is the adiabatic fraction, c_w is the condensation rate, Q_{ext} is the extinction coefficient, and ρ_w is the density of liquid water (Grosvenor et al., 2018).

To facilitate a consistent comparison, the satellite retrievals are adjusted to the same domain size as the simulation (e.g., $1° \times 1°$) and the pixel-level cloud retrievals are smoothed to 25-km resolution to reduce impact from cloud heterogeneity and small-scale covariability on the estimated cloud susceptibility (e.g. Arola et al. 2022; Zhou and Feingold, 2023). In the context of ACI: cloud susceptibility quantifies how sensitive a cloud property responds to change in aerosol concentration or N_d. To constrain the spatial-temporal variation in meteorological conditions and cloud properties, cloud susceptibility is estimated as the regression slope between N_d and cloud properties within the $1° \times 1°$ domain at each time step of satellite observations. In this study, we quantify LWP and cloud fraction (CF) susceptibilities. Because of the non-linear relations between LWP and N_d, the LWP susceptibility is quantified in logarithm scale as $dln(LWP)/dln(N_d)$ (e.g., Gryspeerdt et al. 2019; Qiu et al., 2024), whereas CF susceptibility is quantified as $dCF/dln(N_d)$ (e.g., Kaufman et al. 2005; Chen et al., 2022; Qiu et al., 2024). Due to the dependence of cloud responses on cloud regimes (e.g., Chen et al., 2014; Zhang et al., 2022; Qiu et al., 2024), the estimated cloud susceptibilities are displayed in the N_d-LWP parameter space as the classification of cloud states.

In addition to the satellite retrievals, we adopt the ground-based observation at the ARM ENA site. Specifically, we use the ground-based cloud radar and lidar observations for process-level evaluation of modeled precipitation processes. In this study, the radar reflectivity (Z_e) and cloud boundaries are from the Active Remote Sensing of Clouds (ARSCL) value added product (Clothiaux et al., 2001). To remove noise in the data, we smoothed the 4s reflectivity profiles into 1-minute. Cloud top height is derived as the upper most range gate height with radar reflectivity greater than the sensitivity threshold of the Ka-band zenith radar (-40 dBZ) combined with the hydrometer layer top data in the ARSCL. Cloud base height is from the best-estimate cloud base height variable in the ARSCL product. Thermodynamic profiles are derived from the radiosonde data, which is launched at the ENA site twice daily at 0000 UTC and 1200 UTC.

The ground-based r_e and τ retrievals are based on the parameterization developed in Dong et al. (1998), where r_e is retrieved from a radiative transfer model as described in Dong et al. (1997) and parameterized as a function of cloud LWP, shortwave transmission ratio, and cosine of solar zenith angle. Cloud LWP is retrieved from the brightness temperature measured by the three-channel microwave radiometer (MWR3C) at 23.8, 30, and 90 GHz (Cadeddu et al., 2013). The shortwave transmission ratio is calculated from the unshaded pyranometer from the QCRAD product (Long and Shi, 2006), defined as the ratio between cloudy and clear-sky shortwave irradiance.

Meteorological and thermodynamic variables are extracted from the European Center for Medium-Range Weather Forecasts (ECMWF) ERA5 reanalysis data and used as the forcing for the simulation. ERA5 is the fifth generation of the ECMWF reanalysis, replacing the ERA-Interim reanalysis. ERA5 provides the best-estimate of the global atmosphere, land surface, and ocean waves with a horizontal resolution of 31 km and an hourly output throughout (Hersbach et al., 2020). Atmospheric variables are available on 137 vertical levels, ranging from 1000 hPa (near surface) to 1 Pa (~80km).

2.2 WRF Model

We used the Weather Research and Forecasting (WRF) model version 4.4.2 (Skamarock et al., 2021) for our simulations. In a companion study, Lee et al. (2025) used the WRF model at near LES scale with interactive chemistry and aerosol schemes (WRF-Chem) and investigated ACI and its feedback on both clouds and aerosols in the ENA region. As the WRF-Chem simulations are 5-10 times more computationally expensive, the present study adopted the same dynamical and physical configuration and conducted more experiments with prescribed aerosol concentrations and realistic meteorology.

We employed four one-way nested domains in the model, with the domain size of $27° \times 27°$, $9° \times 9°$, $3° \times 3°$, and $1° \times 1°$, and spatial resolution of 5km, 1.67 km, 0.56 km, and 190m, respectively, for d01, d02, d03, and d04 domain. The innermost domain (d04) exhibit a domain size close to most GCM grid spacing and is consistent with the spatial scale for quantification of cloud susceptibility in satellite study (e.g., Zhang et la., 2022, 2023; Qiu et al., 2024). The spatial resolution of 190m is much higher than the CPMs and close to the LES scale. All the analyses and evaluations in this study are based on output from the innermost domain (d04). There are 75 vertical levels in the model with a model top of ~20 km, the grid spacing is log-stretched with higher resolution of ~50 m near the surface and increases to ~150 m at the height of ~1500m . As mentioned above, the initial and lateral boundary conditions for the outer domain are taken from the ERA5 reanalysis data.

The simulations are performed using the Rapid Radiative Transfer Model for Global Climate Models (RRTMG; Mlawer et al., 1997), and the Noah land surface model (Chen and Dudhia 2001). The Mellor–Yamada–Janjic (MYJ; Mellor and Yamada, 1982) planetary boundary layer (PBL) scheme and the shallow cumulus schemes (Hong and Jiang, 2018) are utilized for the outer domain (d01 and d02) only. Simulations in this study employ a two-moment Morrison microphysics scheme, which has been widely implemented in both CPMs and GCMs (Morrison et al., 2005; Morrison and Gettleman, 2008; Golaz et al., 2022). In the Morrison two-moment microphysics scheme, the DSD (ϕ) is defined as:

$$\phi(D) = N_0 D^{\mu} e^{-\lambda D}, \tag{2}$$

$$\eta = 0.0005714 N_d + 0.2714, \tag{3}$$

$$\mu = \frac{1}{\eta^2} - 1, \tag{4}$$

$$\lambda = \left[\frac{\pi \rho N_c \Gamma(\mu+4)}{6 q_c \Gamma(\mu+1)}\right]^{1/3}, \tag{5}$$

where D is the diameter, N_0 is the intercept parameter, μ is the shape parameter, λ is the slope parameter, η is the dispersion parameter which governs the width of the DSD (Morrison and Gettleman, 2008).

Instead of prescribing a constant cloud droplet number concentration, total aerosol number concentrations are prescribed as a constant throughout the domain with no explicit vertical variation or transport in all simulations. Aerosol activation follows the parameterization of Abdul-Razzak & Ghan (2000), with fixed assumptions for size distribution, chemical composition, aerosol type, and mixing state. The activated fraction mainly depends on the local supersaturation and updraft speed. The fixed aerosol field neglects spatial and temporal variability driven by emissions, long-range transport, wet scavenging, and CCN reactivation from evaporated raindrops. These missing processes can sustain higher CCN concentrations, suppress precipitation, and potentially exaggerate positive LWP responses.

Despite this simplification, our companion WRF-Chem study (Lee et al., 2025) shows that, even with full aerosol microphysics, wet scavenging, and aerosol reactivation, the simulated LWP responses remain broadly consistent with the results presented here, especially the positive susceptibility in precipitating clouds. This agreement suggests that the key findings of this work are robust, although the prescribed-aerosol assumption may still contribute to some of the quantitative discrepancies discussed in Section 3.

For each case, we run the model for 36 hours (except for the consecutive case on 21 July 2016, where the model was run for 60 hours), starting at 12:00 UTC of the previous day and the first 12 hours are used as model spin-up period. The time resolution of the model is 30 seconds in the outer domain for advection and physics calculation and is 1 second for the innermost domain. Model variables are output instantaneously for every 10 minutes for the innermost domain, similar as in satellite observation of snapshots.

To access the cloud responses to aerosol perturbations, we conduct three sets of simulations with different prescribed aerosol number concentration of N=100, 500, and 1000 cm^{-3} for all 11 cases. Cloud susceptibility is quantified as the change in domain-mean cloud properties within the innermost domain at the same output time, comparing polluted and clean simulations (e.g. N=1000 vs. N=100, N=500 vs. N=100, and N=1000 vs. N=500). With constant and uniform aerosol concentration, the N_d-LWP relations resulting from internal cloud processes are able to be quantified within each experiment at the same output time. To minimize N_d-LWP relations from cloud heterogeneity and small-scale covariability and to be consistent with the quantification of cloud susceptibility in satellite observations, the pixel level model outputs are smoothed to 25-km resolution and N_d-LWP relations are quantified as $dln(LWP)/dln(N_d)$ using the smoothed data.

To directly compare the WRF simulations with ground-based observations, we used the Cloud Resolving Model Radar Simulator (CR-SIM; Oue et al. 2020). It is a forward-modeling framework which uses consistent microphysics assumptions as in the atmospheric model (i.e., the two-moment Morrison scheme in this study) and emulates radar and lidar observables. Some common radar and lidar variables include: the radar reflectivity factor at horizontal and vertical polarization, depolarization ratio, Doppler velocity, spectrum width, lidar backscatter, attenuated backscatter, lidar extinction coefficient, and so on. In this study, we analyzed the simulated radar reflectivity factor to characterize cloud and precipitation properties.

To distinguish different precipitation modes and the microphysical growth processes that transition clouds from non-precipitating to drizzling and raining, we investigate the vertical transition from cloud to precipitation using the Contoured Frequency of Optical Depth Diagram (CFODD) method (Suzuki et al., 2010) from both observations and model simulations. The CFODD analysis calculates the frequency of radar reflectivity profiles as a function of in-cloud optical depth (τ_d), where τ_d is calculated based on an adiabatic-condensation growth model and it starts at zero at cloud top and increases downward. One benefit of the CFODD analysis is that the slope of reflectivity directly relates to the droplet collection efficiency, where the slope of reflectivity in the common geometric height depends on cloud water content (Suzuki et al., 2010).

2.3 Case Studies

With the focus of MBL clouds in this study, cases are selected when both satellite and ground-based observations define MBL clouds in the ENA region. For cloud type classification in ground-based observations, we used the same method as in Zheng et al. (2025), where clouds are classified into seven types based on the boundaries and duration of each cloud object. In this study, we include both cumulus and stratocumulus clouds. Days are excluded when only shallow cumulus clouds are detected to filter out clouds that are below the detectable resolution of the Meteosat observations and to minimize uncertainties in the cloud microphysical retrievals from the ground-based observations. We further exclude days with more than three layers of cloud in the boundary layer to minimize uncertainty in cloud retrievals. Classification of cloud type in Meteosat observations uses a similar method as the ground-based observations. Cloud objects are defined as connected cloudy pixels, where low clouds are defined as clouds with 90th percentile of cloud top height below 3km. Low clouds are further classified as stratiform clouds and cumulus or broken stratiform clouds using an area threshold of 10,000 km^2 (Qiu and Williams, 2020).

We focus on summer months (June, July, August) in the ENA region, when this region is often dominated by the Bermuda high-pressure systems and MBL clouds have the highest occurrence frequency (e.g., Li et al., 2011; Mechem et al., 2018; Dong et al., 2014, 2023). Previous studies found that the ARM measurements at the ENA site –located near the northern shore of the Graciosa Island, the northernmost island in the Azores archipelago – can be influenced by local emissions and island effects during southerly wind conditions. These impacts include modification to the aerosol and CCN concentrations, boundary layer turbulence, and the cloud field (e.g., Ghate et al, 2021, 2023). To minimize these influences, we focus on the three synoptic regimes identified in Zheng et al. (2025) when the ENA site is influenced by northerly surface wind: the high-ridge regime (characterized by a mid-tropospheric ridge and surface high-pressure system), the post-trough regime, and the weak trough regime (Table S1, Figure S1).

With the case selection criteria discussed above, there are a total 11 cases for the WRF simulations, covering different cloud states and synoptic conditions. The general characteristics of the 11 cases are listed in Table S1. The synoptic pattern for each case from ERA5 is shown in Figure S1, the cloud fields observed from Meteosat are shown in Figure S2. WRF simulated cloud fields in the N=100 and N=1000 experiments are shown in Figure S3, S4. To better illustrate the large-scale cloud organization and compared with Meteosat observations, the simulated LWP in domain 2 are shown. As seen in Figures S2-4, our WRF simulations well capture the frontal systems and synoptic pattern of cloud fields across different cases.

3 Results:

3.1 Case Study: Impacts of Aerosols on PBL Thermodynamics and Cloud Evolution

Previous studies have demonstrated the distinct cloud responses to aerosol perturbations between precipitating and non-precipitating regimes in both model simulations and observations (e.g., Chen et al., 2014; Sato et al., 2018; Gryspeerdt et al., 2019; Fons et al., 2024; Qiu et al., 2024). To explore these differences, we analyze two representative cases in our simulations: one dominated by precipitating clouds and another by non-precipitating clouds, to highlight the distinct interactions among aerosols, clouds, and PBL thermodynamics in the presence and absence of precipitation.

On 21 July 2016, the ENA site was presented by precipitating stratocumulus clouds from 00:00 UTC to 13:00 UTC, as seen from radar reflectivity profiles in Figure S5b. The clouds dissipated from 12- 18 UTC and redeveloped after 18 UTC (Figure 1a, black line). The sounding observations show a moist and well-mixed boundary layer, with relative humidity (RH) near saturation above cloud top (Figure S6). Our simulation captures the structure of the boundary layer, with a moist layer above the cloud, and the cloud-top RH close to sounding observations (99% and 96%, Figure S6c). Due to biases in the ERA5 reanalysis in representing the temperature inversion, the boundary layer top in the model is ~500m lower than in sounding data (Figure S6). Consequently, the simulated cloud tops are ~300–500 m lower than both satellite and ground-based radar observations (Figure 1b, Figure S6).

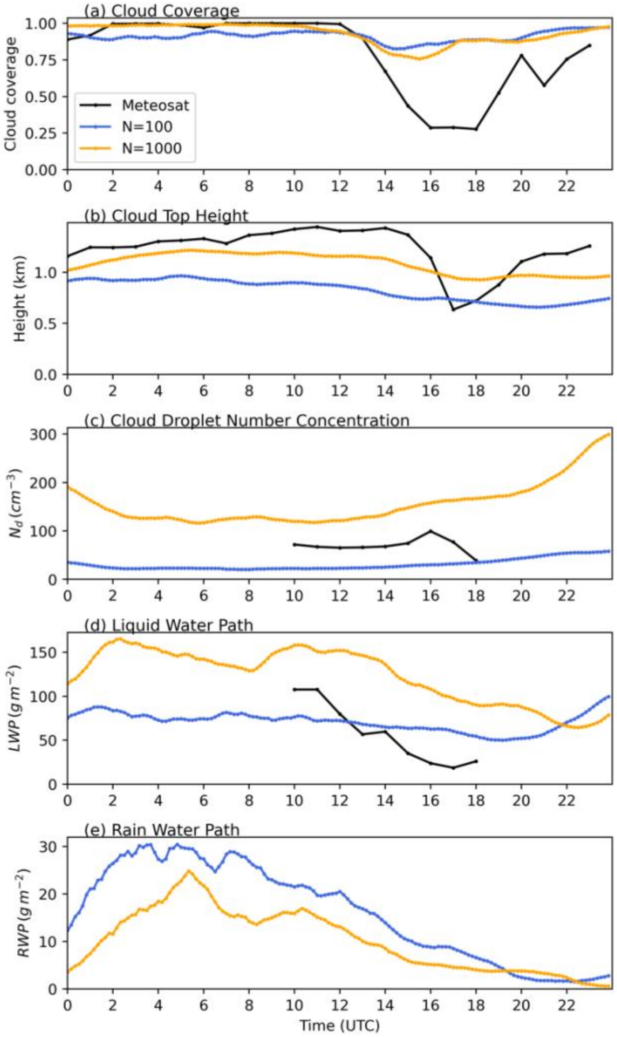

Figure 1. Time series of domain-averaged cloud properties from satellite observations and model simulation on 21 July 2016. (a) Cloud coverage, (b) cloud top height, (c) cloud liquid water path, and (d) rain-water path for N=100 (blue lines) and N=1000 (orange lines) experiments.

In the N=100 simulation, WRF model reproduces the overcast and precipitating stratocumulus clouds, with a domain mean cloud cover varies between 0.90 to 0.94 from 00-13 UTC, which is slightly below that from Meteosat of 0.97 to 1.0 (Figure 1a, blue and black lines). However, unlike observations, the simulated clouds do not dissipate after 14 UTC; both cloud cover and LWP remain nearly constant throughout the day (Figures 1a, d, blue lines). With increased aerosol concentration (N=1000), the simulated precipitation is suppressed (Figure 1e), and the cloud layer remains overcast while deepening, accompanied by rising cloud tops and increasing LWP (Figure 1b, c, orange lines). This cloud response arises from aerosol-induced precipitation suppression and the corresponding changes in boundary layer processes, as illustrated in Figure 2. The turbulent kinetic energy (TKE) is calculated as $\frac{1}{2}\left(\overline{u'^2}+\overline{v'^2}+\overline{w'^2}\right)$, with a unit of m^2s^{-2}, and buoyancy flux is calculated as $g/\theta_0\overline{w'\theta_v'}$, with a unit of m^2s^{-3}.

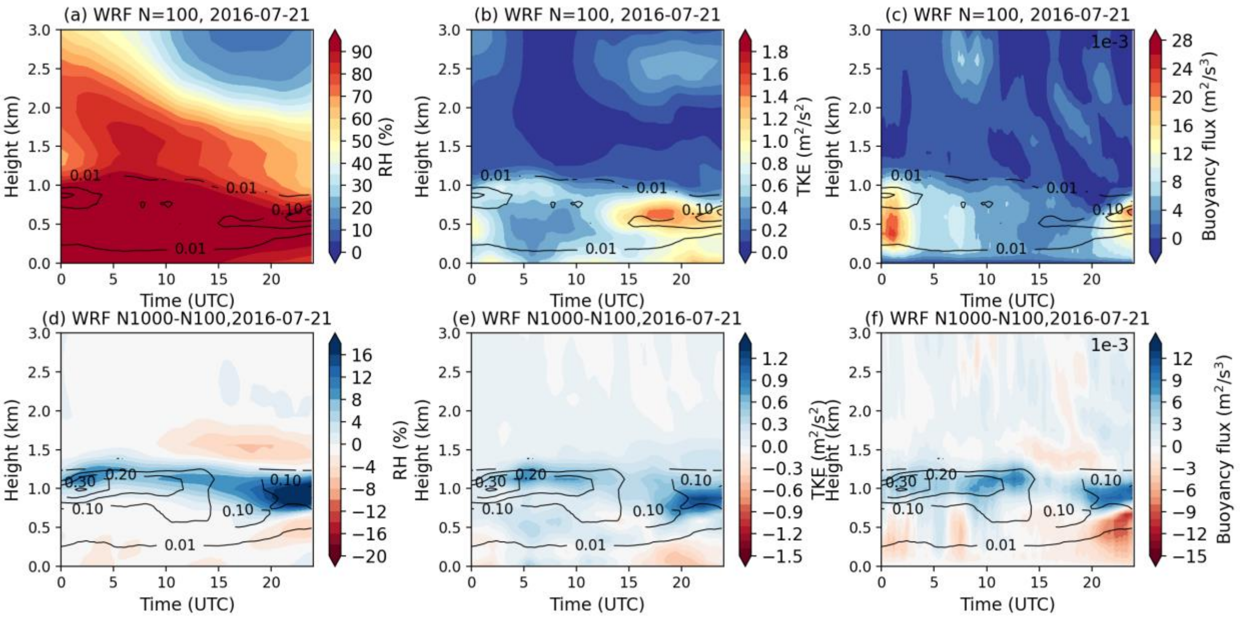

Figure 2. Time series of domain-averaged thermodynamic profiles on 21 July 2016, for (a) relative humidity, (b) turbulent kinetic energy (TKE) (unit: $m^2 s^{-2}$), (c) buoyancy flux (unit: $m^2 s^{-3}$) in N=100 simulations, (d) changes in relative humidity profiles, (e) changes in TKE, (f) changes in buoyancy flux between N=100 and N=1000 simulations. The black contours are cloud water mixing ratio (unit: g/kg) in (a)-(c) N=100 and (d)-(f) N=1000 simulations.

In the simulations, increases in aerosol concentrations lead to higher N_d and smaller drop size. As the two-moment Morrison scheme does not consider the cloud drop size in the parameterization of evaporation, aerosol impacts on clouds and boundary layer occur through the influence of precipitation on PBL structure. Specifically, aerosols suppress precipitation by reducing autoconversion with increasing N_d, decreasing sedimentation rate and terminal velocity from smaller droplets. The formation of drizzle release latent heat and reduce both entrainment and the production of turbulent kinetic energy (TKE) by buoyancy; while the evaporation of drizzle below cloud cool and moisten the sub-cloud layer that decrease buoyancy and TKE (Stevens et al., 1998). As a result, the reduced precipitation increases both TKE and buoyancy flux in the cloud layer and below cloud (Figure 2e, f). The enhanced turbulence and buoyancy support vertical development of clouds, raising cloud tops and expanding the cloud layer upward (Figures 1b and 2), while also increasing RH near the cloud top (Figure 2d).

On the second day (22 July 2016), the precipitating stratocumulus clouds transition into non-precipitating thin stratus over the ENA site (Figure S7). The clouds were predominately overcast from 00-09 UTC and dissipated after 10 UTC, with the domain-mean cloud coverage decreasing from 0.8-0.9 to 0.1-0.2 (Figure 3a, black line). As shown in Figure S8, the boundary layer was moist and well-mixed, capped by a sharp temperature inversion, and moisture decreases rapidly above the inversion. WRF model reproduces the general thermodynamic structure, including the inversion and moisture decline above the PBL. However, due to biases in ERA5 thermodynamic profiles, the simulated PBL top is about 700m lower than observed (Figure S8). Additionally, WRF model fails to capture the rapid decrease of moisture above cloud top, resulting in a more humid layer above cloud with cloud-top RH of 87% in the model, compared to 62% in sounding observation (Figure S8c).

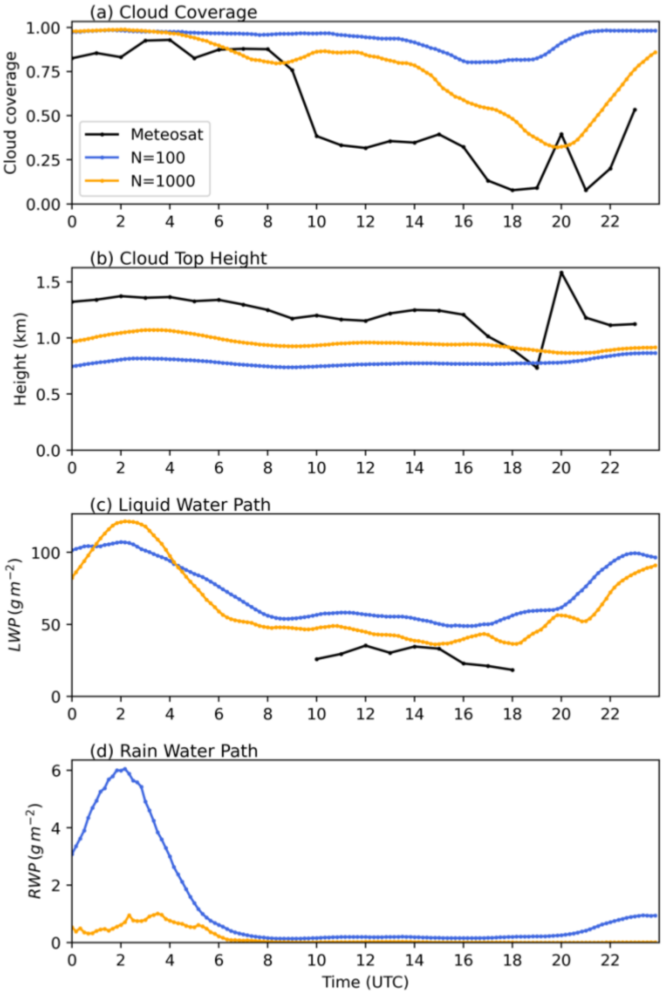

Figure 3. Time series of domain-averaged cloud properties from observations and model simulation on 22 July 2016. (a) Cloud coverage, (b) cloud top height, (c) cloud liquid water path, and (d) rain-water path for N=100 (blue lines) and N=1000 (orange lines) experiments.

In the N=100 simulation, the simulated stratocumulus cloud generates light precipitation from 00-06 UTC, then it transitions to a non-precipitating thin cloud layer after 06 UTC (Figure 3d, blue line). However, the cloud does not dissipate in the model. Domain-mean cloud cover remains between 0.85 to 0.95 throughout the day, and the simulated LWP is nearly twice that retrieved from Meteosat (Figure 3a and 3c, blue lines). When aerosol concentrations are increased to N=1000, clouds dissipate from 14-20 UTC, with a decreasing domain-mean cloud cover and becoming more consistent with observations (Figure 3a, orange line). Meanwhile, cloud tops rise slightly with increasing aerosol. The cloud dissipation reflects a net effect of aerosol induced changes in condensation, evaporation, turbulence, and buoyancy, as shown in Figure 4.

During the early phase (00–06 UTC), increased aerosol loading suppresses drizzle, leading to an increase in LWP and a decrease in RWP (Figure 3c, d). Similar as the first case, the suppressed precipitation enhances turbulence and increases TKE in and below cloud (Figure 4e), lift the cloud top, and lead to an increase in RH near cloud top (Figure 4d). Meanwhile, the free tropospheric air above cloud top is relatively drier compared to the first case (Figure 4a). The increased turbulence and raised cloud top entrain dry air into the cloud and enhances evaporation. After 6 UTC, as clouds become non-precipitating in the N=100 experiment, the decrease of cloud water from evaporation starts to dominate the increase from precipitation suppression and lead to a net decrease in LWP. Reduced buoyancy weakens the upward transport of moisture and energy from the sub-cloud layer, further contributing to cloud dissipation. As a result, both cloud cover and LWP decrease with increasing aerosol. (Figure 3a, c).

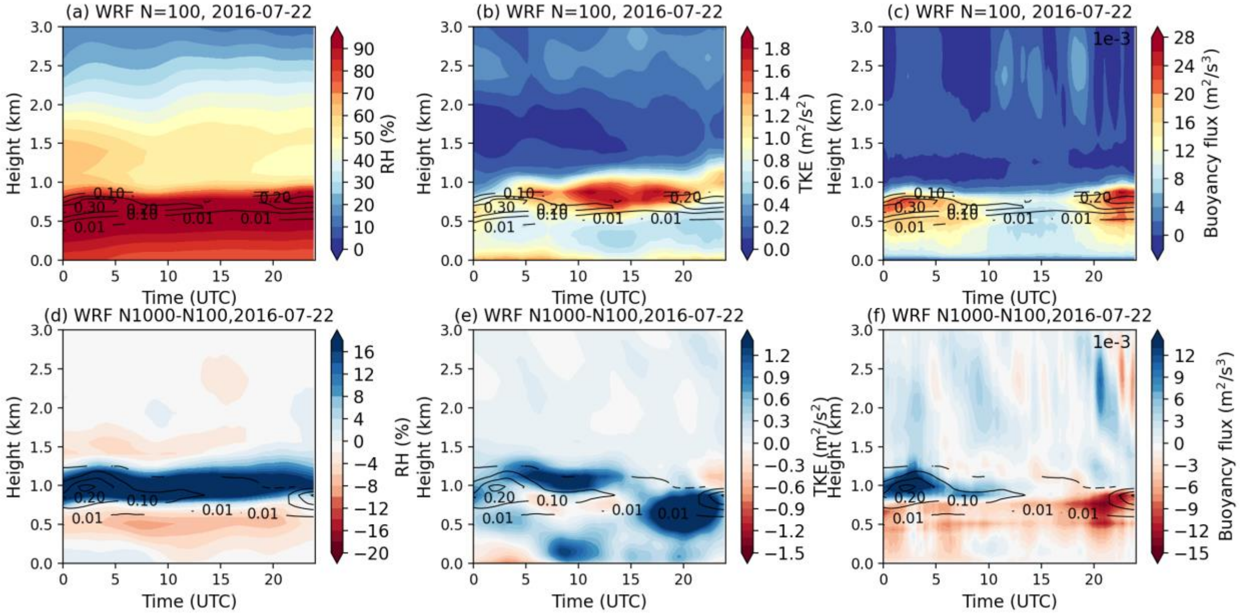

Figure 4. Time series of domain-averaged thermodynamic profiles on 22 July 2016, for (a) relative humidity, (b) turbulent kinetic energy (TKE) (unit: m^2s^{-2}), (c) buoyancy flux (unit: m^2s^{-3}) in N=100 simulations, (d) changes in relative humidity profiles, (e) changes in TKE, (f) changes in buoyancy flux between N=100 and N=1000 simulations. The black contours are cloud water mixing ratio (unit: g/kg) in (a)-(c) N=100 and (d)-(f) N=1000 simulations.

The absence of afternoon cloud dissipation in WRF simulations are likely associated with model biases in the thermodynamic structure inherited from ERA5. For example, on 21 July 2016, ARM sounding observations show a pronounced decrease in specific humidity and relative humidity above the PBL between 14 and 20 UTC (figures not shown). This sharp drying leads to cloud erosion in the observations. However, WRF simulations or ERA5 reanalysis produces only a gradual reduction in moisture from 00 to 20 UTC (Figure 2a), maintaining a moist layer above cloud top and prevent cloud breakup. On 22 July 2016, the model reproduces the moisture gradient above PBL with a warm and dry layer above, the lifted cloud top in the N=1000 simulation entrain dry air into cloud system and dissipate clouds in the afternoon (Figure 3a). On days when ERA5 accurately capture the observed moisture decrease above PBL (e.g., 25 and 28 July 2016), the model reproduces both the dissipation and evening redevelopment of clouds seen in Meteosat data (figures not shown). This indicates that the diurnal evolution of MBL clouds is highly sensitive to the representation of diurnal variation in moisture as well as the moisture gradients near the inversion.

The prescribed, vertically uniform aerosol concentration further reinforces cloud persistence by maintaining elevated CCN levels and suppressing drizzle formation. The lack of precipitation scavenging prevents cloud-base evaporative cooling and inhibits decoupling, both of which would otherwise promote afternoon cloud breakup. The implications of thermodynamic biases (e.g. the moist layer above cloud top and the underestimated PBL height) for the estimated ACI are discussed in detail in Section 3.3.2

In a nutshell, precipitating and non-precipitating clouds react differently to aerosol perturbations in our simulations. For precipitating clouds, aerosols increase LWP through precipitation suppression and support vertical development of cloud through the impact of precipitation on PBL dynamic and thermodynamics. For the non-precipitating case, PBL air is drier compared to the first case, the enhanced turbulence and entrainment of dry air above leads to evaporation and reduced buoyancy. The reduced buoyancy stabilizes PBL and decays the cloud layer.

3.2 Evaluation of LWP Susceptibility Across Cloud States and Synoptic Conditions

The two cases in Section 3.1 demonstrate the impact of different cloud states and PBL thermodynamics on cloud responses to aerosol perturbations. In order to evaluate the ACI process across all simulated cloud states, we composite the cloud fields from all 11 cases and all three aerosol concentrations (e.g. N=1000 vs. N=100, N=500 vs. N=100, and N=1000 vs. N=500) to estimate the mean LWP response, and compare it with satellite retrievals, as shown in Figure 5. More specifically, LWP susceptibility in WRF simulations is defined as the change in domain mean cloud properties as $dln(LWP)/dln(N_d)$ between polluted and clean simulations for each 10-minutely model output. To be consistent with satellite retrievals, we focus on daytime with solar zenith angle less than 65°. Lastly, we use the LWP-N_d parameter space to represent different cloud states. (Qiu et al., 2024).

Based on the relationships between r_e, LWP, and N_d in the satellite retrievals (e.g., $LWP = \frac{4 r_e \tau}{3 Q_{ext}}$, $N_d = \frac{\sqrt{5}}{2\pi k}(\frac{f_{ad} c_w \tau}{Q_{ext} \rho_w r_e^5})^{1/2}$), r_e =15 isolines is marked in the LWP-N_d parameter space as an commonly used indicator of precipitation likelihood in the satellite retrieval (e.g., Gryspeerdt et al., 2019; Toll et al., 2019; Zhang et al., 2022; Qiu et al., 2024). Based on the distinct LWP, cloud albedo and CF susceptibilities between cloud states, MBL clouds are classified into three states: the precipitating clouds (r_e >15 μm), the non-precipitating thick clouds (r_e <15 μm, LWP> 75 gm^{-2}), and the non-precipitating thin clouds (r_e <15 μm, LWP< 75 gm^{-2}) (Qiu et al., 2024). To be consistent with observational reference, the WRF simulated cloud states are classified using the same definition. Similar to warm MBL clouds in observations (e.g. Qiu et al., 2024), LWP responses to aerosol perturbation in model simulations show clear dependence on cloud state (Figure 5a).

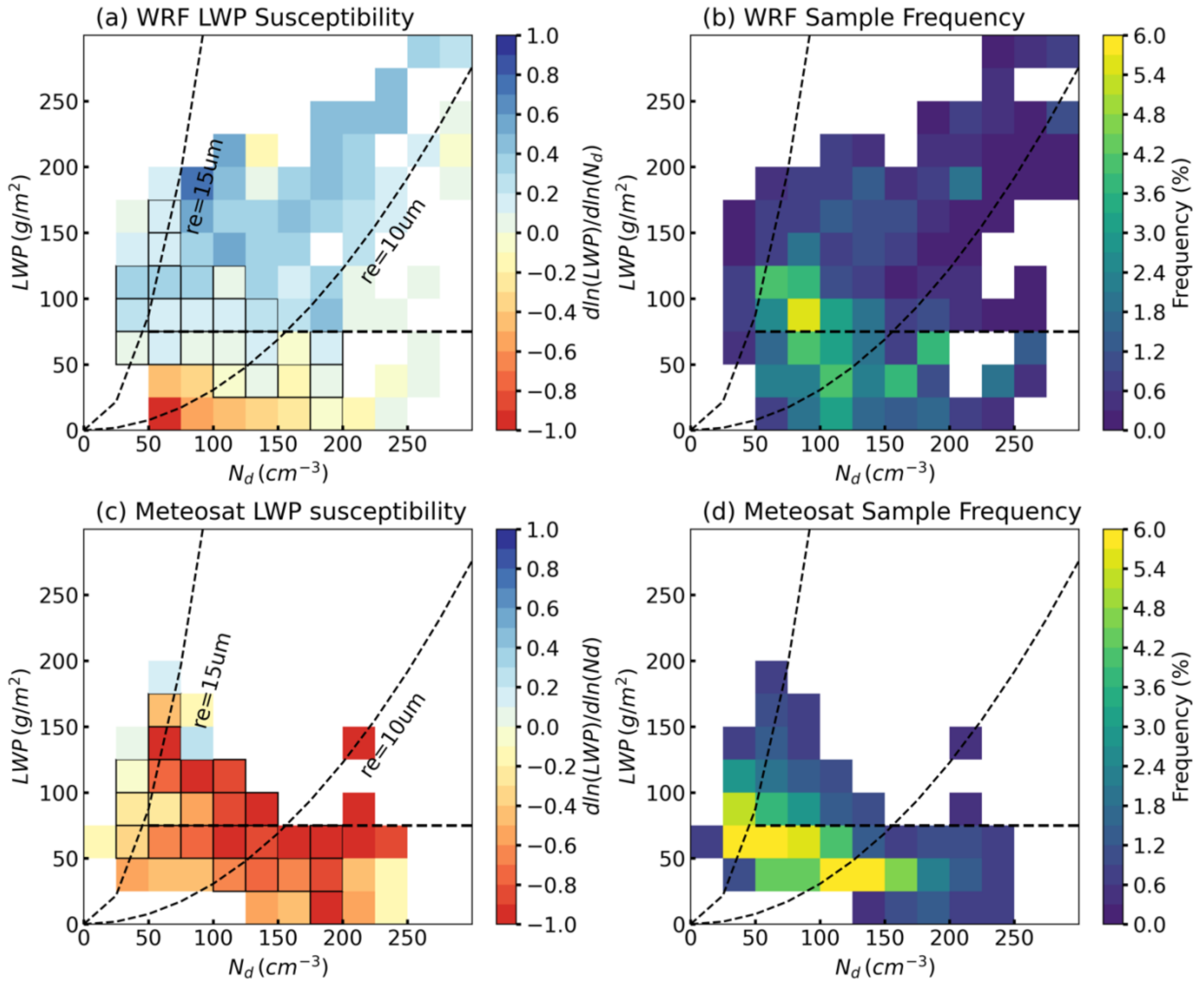

Figure 5. Mean liquid water path (LWP) susceptibility from (a) (b) WRF simulations and (c) (d) Meteosat cloud retrievals during the daytime. (a) (c) cloud LWP susceptibility $dln(LWP)/dln(N_d)$, (b) (d) frequency of occurrence of sample in each bin. The dashed lines indicate $r_e = 15$ μm, $r_e = 10$ μm, and LWP= 75 gm^{-2}, as r_e thresholds for precipitation (precipitating clouds located to the left of the line), and for thick clouds (with LWP > 75 gm^{-2}), respectively. Black-outlined bins denote cases where the WRF and Meteosat LWP susceptibilities differ significantly ($p < 0.05$) based on a Welch's t-test.

For precipitating clouds ($r_e > 15$ μm), LWP slightly increases with N_d, with a mean susceptibility of +0.15. The increase of LWP agrees with the precipitation suppression mechanism. Meanwhile, there are only 4% of clouds in model simulations locate to the left of the $r_e = 15$ μm isotherm with small N_d, even with aerosol concentration set to 100 cm^{-3}(Figure 5b). The non-precipitating thick clouds ($r_e < 15$ μm, LWP> 75 gm^{-2}) is the dominant cloud state in model simulation, with a total frequency of occurrence of 49%. Different from the evaporation-entrainment feedback mechanism, LWP largely increases in the model with increasing aerosols, with a mean susceptibility of +0.32. For non-precipitating thin clouds ($r_e < 15$ μm, LWP< 75 gm^{-2}), LWP decreases with aerosol perturbations with a mean of −0.14, which is consistent with the second case shown in the previous section.

To evaluate model performance, we estimated LWP susceptibility from satellite retrievals within the same domain and for the same 11 cases as the model simulations (Figures 5 c, d). Specifically, LWP susceptibility was quantified as the regression slope between LWP and N_d within the 1° × 1° domain at each time step of satellite observations. For precipitating clouds, LWP slightly decreases with increasing N_d in satellite data, consistent with the four-year climatological mean feature in the ENA region reported in our previous study (Qiu et al., 2024). This decrease of LWP with increasing N_d is likely associated with the depletion of LWP through sedimentation–evaporation–entrainment feedbacks, which outweigh the increase of LWP from precipitation suppression. In contrast, in model simulations, the lack of realistic evaporation-entrainment feedback results in LWP increasing primarily through precipitation suppression. The simulated LWP susceptibilities are significantly different with satellite observations at 95% confidence level for most precipitating clouds (Figure 5a).

For non-precipitating thin clouds, the simulated decrease in LWP with increasing aerosol concentration agrees in sign with satellite observations. However, the magnitude of this decrease is weaker, and the simulated susceptibilities remain significantly different from satellite estimates at 95% confidence level for most bins (Figure 5a, c). This model behavior contrast with most GCM and coarse CPM studies, which often simulate an increase of LWP for non-precipitating clouds (e.g., Fons et al., 2024; Christensen et al, 2024; Mülmenstädt et al., 2024;). The improved representation in our high-resolution simulations arise from better-resolve PBL turbulence and thermodynamics, which enhance the entrainment of dry air, accelerates evaporation, reduces buoyancy, and promotes dissipation of the cloud system.

In contrast, for non-precipitating thick clouds, the model and observations diverge substantially. In satellite observations, LWP decreases most strongly for this cloud state, with a mean LWP susceptibility of -0.69 (Figure 5c). This observational estimate is consistent with the climatological mean derived from four years of Meteosat data over the ENA region (Qiu et al., 2024). In the model, however, LWP increases most strongly with increasing N_d for this cloud state. Moreover, compared with satellite retrievals, model simulates substantially larger population of polluted thick clouds characterized by high N_d and LWP. For example, non-precipitating thick clouds are the dominant cloud state in the model, accounting for 49% of total cloud occurrence (Figure 5b), whereas they are the least frequent in observations, at only 15.7% (Figure 5d). Meanwhile, only 4% of simulated clouds fall into the precipitating cloud regime with $N_d < 50$, compared to a 22.2% in the satellite observations

The overall overestimation of N_d likely arises from the prescribed aerosol concentration in the model configuration, combined with the absence of precipitation scavenging. For reference, the mean aerosol concentration over the ENA region during summer is approximately 400 cm^{-3} (e.g., Zhang et al., 2021; Wang et al., 2021; Zheng et al., 2024). The model's overestimation of LWP may stem from its excessively positive LWP susceptibility in thick clouds. As shown in Figure S9, simulated LWP in the N=100 experiment agrees reasonably well with the Meteosat retrievals, with a mean value about 10% lower than observed. However, in the N=500 and N=1000 simulations, the strong positive LWP susceptibility leads to increases in LWP for clouds with LWP> 75 gm^{-2}, resulting in mean values 30% and 40% higher than Meteosat retrievals, respectively.

To further examine whether these discrepancies depend on large-scale meteorological conditions, we assessed LWP susceptibility across different synoptic regimes. Because only one case is available for the "weak-trough" regime (Table S1), our comparison focuses on the "high-ridge" and the "post-trough" regimes (Figure S10). The "high-ridge" regime shows a higher occurrence of non-precipitating thin clouds than the “post-trough” regime, with total frequencies of 49% and 40%, respectively (Figures S10b, d). This more frequent non-precipitating thin cloud in the model is consistent with our previous study based on six years of ground-based observations at the ARM ENA site, which revealed that the “high-ridge” regime favors single-layer stratocumulus clouds with shallower cloud depth and smaller LWP compared to the “post-trough” regime (Zheng et al., 2025).

In addition, non-precipitating thin clouds in the “high-ridge” regime exhibit more negative LWP susceptibilities than clouds with similar LWP and N_d in the “post-trough” regime. This difference in LWP susceptibility is associated with the colder and drier air above clouds under subsidence in the “high-ridge” regime, which facilitates cloud dissipation, as also demonstrated in the case study. Furthermore, non-precipitating or lightly drizzling thick clouds in both synoptic regimes manifest strong positive LWP susceptibilities, suggesting that the model-observation discrepancy for this cloud state persist regardless of synoptic conditions and therefore warrants further investigation. In summary, the mean LWP susceptibility from our simulations were evaluated against satellite retrievals in the LWP-N_d parameter space across different cloud states and synoptic conditions for a comprehensive comparison. The simulations reproduce the observed decrease in LWP for non-precipitating thin clouds, although with weaker magnitudes. For precipitating clouds, the model predicts a slight increase in LWP instead of the weak decrease seen in satellite observations, reflecting the limited representation of evaporation-entrainment feedback in the model. Large discrepancies remain for non-precipitating or lightly drizzling thick clouds, where the model simulates too many polluted thick clouds and yields an opposite (positive) LWP response compared to the strongly negative satellite signal.

In addition, the model-observation discrepancy persists across all synoptic regimes, suggesting that they originate from the model’s representation of cloud microphysics, precipitation, and aerosol-cloud coupling rather than from large-scale meteorological variability. The consistency of these modeled LWP response, in agreement with previous LES studies of similar cloud regimes (e.g., Wang et al., 2020; Lee et al., 2025), further motives the central focus of the next section: diagnosing the physical mechanisms driving these biases. We show that three leading factors dominate the discrepancy: excessive precipitation production in thick clouds, a moist bias above cloud top, and satellite retrieved N_d-LWP relationships contaminated by internal cloud processes.

3.3 Causes of Satellite–Model Discrepancies in LWP Susceptibility

The satellite–model differences highlighted above point to systematic biases in how the model represents cloud microphysics, precipitation processes, and entrainment pathways. In this section, we diagnose the physical mechanisms driving these discrepancies, beginning with the model’s precipitation efficiency.

3.3.1 Precipitation Efficiency

A long-standing challenge in numerical models is the tendency to produce precipitation too frequently and too lightly (Sun et al., 2006; Stephens et al., 2010). To assess the modeled precipitation efficiency with observation, Figure 6 shows the mean cloud properties from Meteosat observations, and from WRF simulations for the 11 cases combining all three aerosol concentrations (N=100, 500, and 1000). As satellite retrieves r_e near cloud top, we used r_e at ~100 m below cloud top in the simulation, which approximate $\tau = 2$ from cloud top for marine stratocumulus. The modeled pixel-level precipitation fraction is calculated as the area fraction of cloudy pixels with the column maximum radar reflectivity ($Z\ \ max$) greater than -15 dBZ at each model output time (Haynes et al., 2009; Suzuki et al., 2015; Jing et al., 2017). Modeled radar reflectivity is from the radar simulator (CR-SIM), as discussed in the methodology. The precipitation fraction in Meteosat is calculated as the area fraction of clouds with $r_e > 15\ \mu m$. Qiu et al. (2024) evaluated different effective radius thresholds and rain rate thresholds in satellite retrievals using precipitation masks derived from ground-based radar reflectivity at the ENA site, and concluded that the $r_e > 15\ \mu m$ threshold showed the best agreement with observations.

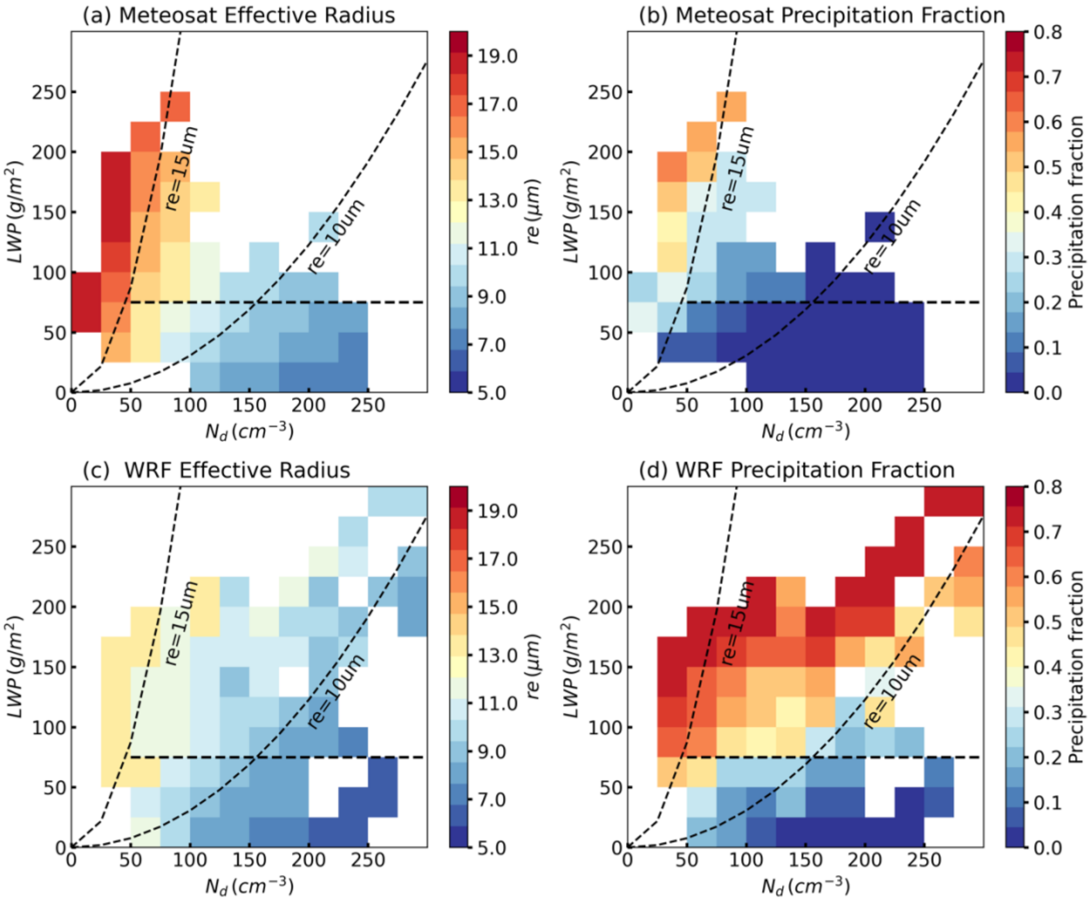

Figure 6. Mean cloud properties from (a), (b) Meteosat retrievals and (c), (d) WRF simulations during the daytime. (a), (c) effective radius, (b), (d) pixel-level precipitation fraction. The dashed lines indicate r_e =15 μm, r_e =10 μm, and LWP= 75 gm^{-2}, as r_e thresholds for precipitation (precipitating clouds located to the left of the line), and for thick clouds (with LWP > 75 gm^{-2}), respectively.

As shown in Figures 6a, c, the modeled r_e is ~1-3 μm smaller than satellite retrievals for a similar cloud condition. Additionally, compared to observation, model generates precipitation too often at smaller drop size with $r_e > 10\ \mu m$ and at higher N_d concentration (Figures 6b, d, r_e =10 μm dashed line). The large discrepancy in LWP susceptibility for thick clouds between the 10 and 15 μm isolines is likely linked to model bias in precipitation efficiency. To further investigate the model bias of excessive rain at smaller drop size and the positive LWP responses to aerosol perturbations, we compared the modeled radar reflectivity profiles from the radar simulator with ARM observations using the CFODD framework. Based on the relationship between Z_e and the droplet collection efficiency (E_c), the vertical slope of Z_e as a function of in-cloud optical depth (τ_d) is directly linked to E_c, a steeper slope indicates a larger E_c (Suzuki et al., 2010).

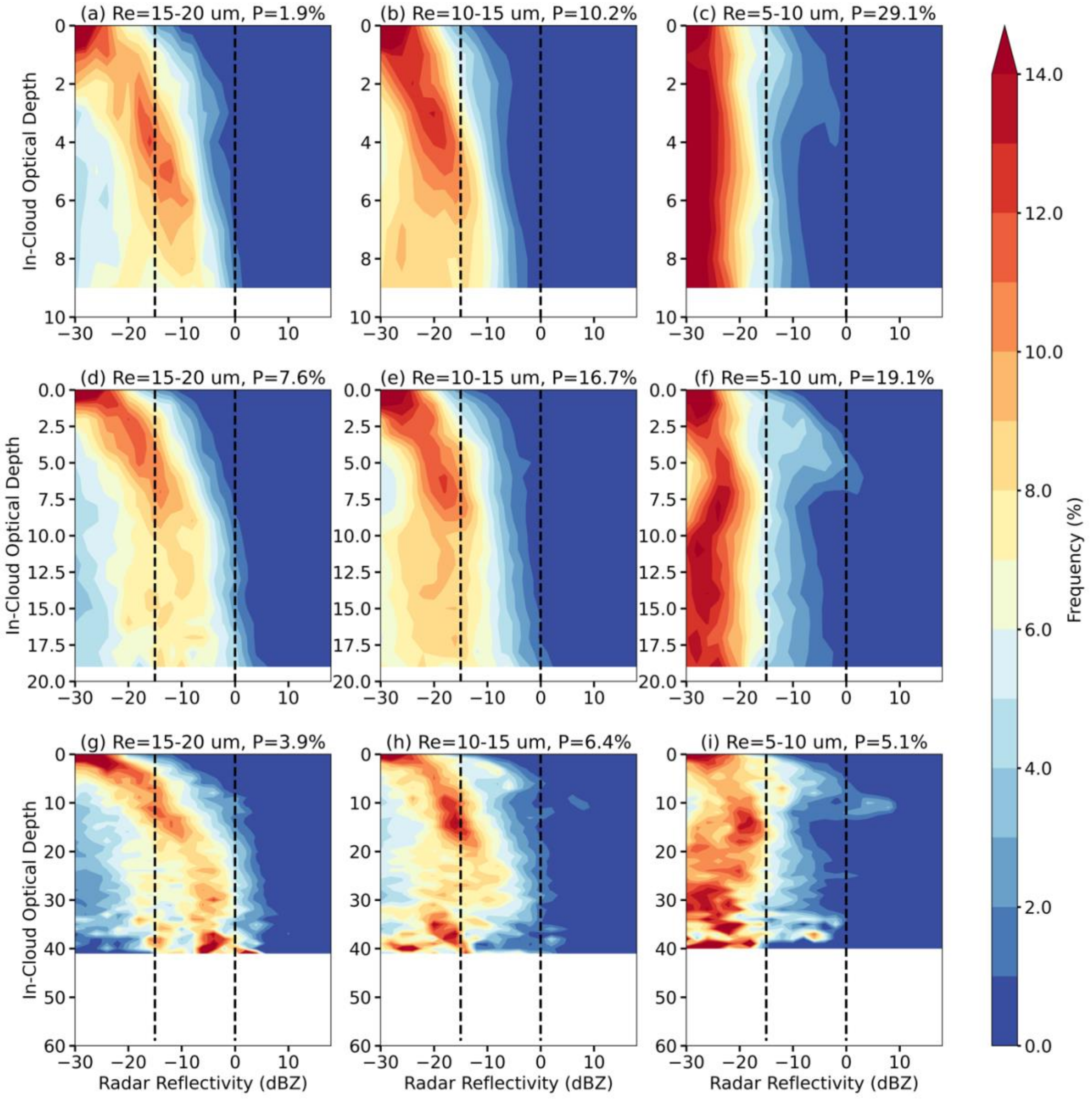

Figure 7. Frequency of radar reflectivity as a function of in-cloud optical depth (τ_d) for ARM ground-based observations during the daytime. Different rows are for different ranges of optical depth (τ): (a)-(c) clouds with $\tau < 10$, (d)-(f) clouds with $10 < \tau < 20$, (g)-(i) clouds with $\tau > 20$. Different columns are for different ranges of effective radius (r_e). The left, middle, and right columns are for $15-20\ \mu m$, $10-15\ \mu m$, and $5-10\ \mu m$, respectively. The black dashed lines in each panel denote -15 dBZ and 0 dBZ, as thresholds of drizzle and rain, respectively. The percentage of sample (P) for each subgroup is denoted in the figure, with a total sample of 91,737.

Ground-based radar reflectivity profiles and cloud retrievals at the ARM ENA site are used as the ground truth. To reduce noise, radar reflectivity profiles and cloud boundary data are smoothed to a 1-minute resolution. To increase the sample size, we analyzed the climate-mean radar reflectivity profiles of stratocumulus and cumulus clouds observed during the summer months (June to August) from 2016 to 2021, comprising a total of 91,737 profiles. Radar reflectivity profiles derived from the selected 11 cases exhibit consistent characteristics (figure not shown). To better distinguish microphysical processes such as autoconversion and accretion from dynamical processes such as updraft, clouds are further categorized by both r_e and τ ranges. MBL clouds are classified as non-precipitating clouds, drizzle, and rain using a reflectivity threshold of $Z\ \ e$ < -15 dBZ, -15 dBZ < $Z\ \ e$< 0 dBZ, and $Z\ \ e$ > 0 dBZ, respectively, as denoted by black dashed lines in Figures 7 (Haynes et al., 2009; Suzuki et al., 2015; Jing et al., 2017).

Applying the same cloud state classification as in the satellite observations (e.g., $r_e >$ 15 μm for precipitating clouds and LWP > 75 gm^{-2} for thick clouds), the total frequency of occurrence of precipitating, non-precipitating thin, and non-precipitating thick clouds are 30.7%, 46.3%, and 23.0%, based on six-year of ARM observations. These frequencies are consistent with those derived from satellite data for the 11 cases (22.2%, 55.6%, and 22.2%, respectively; Figure 5d). Therefore, the selected cases in this study are representative of the typical distribution of MBL cloud types in the ENA region during summer.

As shown in the first column of Figure 7, in clean environment with $\mathrm{r_e} > 15\ \mathrm{\mu m}$, the observed MBL clouds start to drizzle with $Z\ \ e > -15$ dBZ even in the thinnest category (Figure 7a), of which the cloud top is mostly non-precipitating ($Z_e < -25$ dBZ). Cloud drops rapidly grow from cloud top downward and initiate drizzle at ~ 4-6 optical depth into the cloud. However, most observed MBL clouds, even for the thickest category (Figure 7g), remain drizzling rather than raining as most of the radar reflectivity is lower than 0 dBZ.

Figures 7b, e, h represent clouds with observed r_e of $10 - 15\ \mu m,$ indicating an increase in N_d compared with clouds with similar τ and r_e > 15 um (Figures 7a, d, g). Precipitation in these clouds is suppressed as the Z_e is mostly less than –15 dBZ in thin clouds (τ < 10, Figures 7b). Thick clouds produce drizzle at $\sim\tau_d > 20$ and Z_e slightly decrease at cloud base, likely due to mixing and evaporation (Figure 7h). When r_e decreases to below $10\ \mu m$ (Figures 7c, f, i), Z_e further reduces to around –20 to –30 dBZ throughout the cloud layer, indicating that precipitation is further suppressed. The precipitation suppression effect is shown not only by the peak frequency of Z_e, but also the slope of Z_e, which indicates the droplet collection efficiency as discussed above. As seen in Figure 7, for clouds with similar thickness, the slope of Z_e decreases with decreasing r_e, which reflects a weaker collision coalescence and accretion processes with higher N_d and smaller cloud drops.

In thick clouds with $r_e < 10\ \mu m$ (Figure 7i), most radar reflectivity remains below –25 dBZ in the lower cloud layer, while reflectivity slightly increases toward cloud top in the region corresponding to ~10-20 optical depth into the cloud. Reflectivity then decreases again toward cloud top. This vertical pattern is consistent with the structure of marine clouds reported in Suzuki et al. (2010). The observed decrease of reflectivity near cloud top may be attributed to entrainment and evaporation, or to the accretion process involving large droplets falling downward, as indicated by localized reflectivity peaks exceeding -15 dBZ (Figure 7i). Meanwhile, in clouds with small drop sizes, cloud deepening or dynamical processes have little effect on precipitation based on observations.

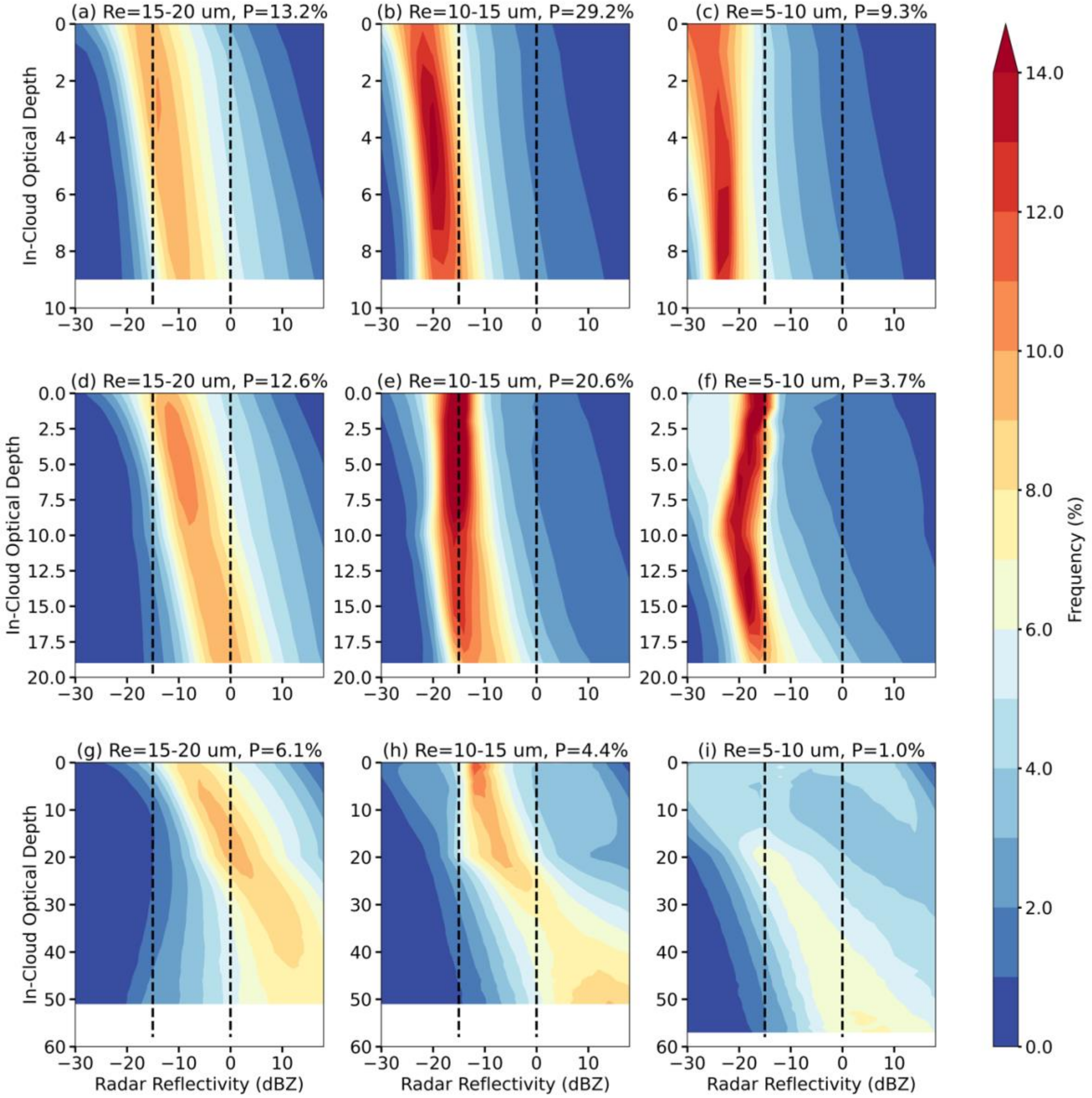

Figure 8. Frequency of radar reflectivity as a function of in-cloud optical depth (τ_d) for WRF N=100 simulation. Different rows are for different ranges of optical depth (τ): (a)-(c) clouds with τ < 10, (d)-(f) clouds with 10< τ < 20, (g)-(i) clouds with τ > 20. Different columns are for different ranges of effective radius (r_e). The left, middle, and right columns are for $15-20\ \mu m$, $10-15\ \mu m$, and $5-10\ \mu m$, respectively. The black dashed lines in each panel denote -15 dBZ and 0 dBZ, as thresholds of drizzle and rain, respectively. The percentage of sample (P) for each subgroup is denoted in the figure.

Compared to the “ground truth”, our model simulations reasonably identify the non-precipitating regime in clouds with $r_e < 10\ \mu m$ and τ < 20, when cloud drops are too small for efficient collision coalescence (Figures 8c, f). Additionally, drizzle initiates at the same r_e and τ ranges as in observations: for example, the maximum frequency of Z_e exceeds -15 dBZ in thin clouds with $r_e > 15\ \mu m$ and τ < 10 (Figure 8a) or in thick clouds with $r_e = 10-15\ \mu m$ and $\tau =$

$10-20$ (Figure 8e). This result is different from GCM or GCPM where models hardly simulate any non-precipitating clouds, or drizzle initiate too early in the cloud (e.g. 5-10 optical depth; Jing et al. 2017, 2019; Michibata and Suzuki, 2020). The better resolved non-precipitating regime as well as the transition from non-precipitating cloud to drizzle process in our simulations reveal the importance of model resolution to better simulate precipitation.

On the other hand, model overestimates precipitation in both intensity and the frequency of occurrence in optical thick with $\tau > 20$, the simulations produce rain with peak Z_e exceeding 0 dBZ in all size ranges, even in clouds with $r_e < 10\ \mu m$ (Figure 8 g-i). Furthermore, precipitation initiates too early near cloud top: all precipitating clouds in the model start to drizzle or even rain at cloud top (Figures 8a, d, e, g, h, i). Based on the features shown in the CFODD analysis, the overestimation of precipitation could be attributed to the following four aspects in the parameterization.

First, the overestimation of reflectivity at cloud top indicates that autoconversion is activated too early in clouds near the top. With the same aerosol concentration, clouds with less activated N_d exhibit larger r_e (Figure 6c). As the autoconversion rate scaled non-linearly with N_d (e.g. $\frac{\partial q_c}{\partial t} = 1350 q_c^{2.47} N_d^{-1.79}$), clouds with larger drop size (e.g. ~15–20 μm) have smaller N_d, and therefore exhibit larger autoconversion rate. Second, the overestimation of reflectivity near cloud top could be due to underestimation of entrainment rate or evaporation rate from the moist layer above. As seen in Figure 8, the simulated Z_e does not decrease towards cloud top or cloud base as in the observations, which indicates an underestimation of entrainment and evaporation. Third, the overproduction of rain in the model indicates an overestimation of the accretion process. In the Morrison scheme, accretion is parameterized as a function of cloud water and rainwater content; thus, when autoconversion is triggered too early, accretion also initiates too early. This bias is amplified in thick clouds, which have greater liquid water content and longer path for droplet collection (Figures 8 g-i). For thick clouds with small drop size (Figure 8i), they remain non-precipitating at the cloud top, indicating that autoconversion is appropriately suppressed by small drop size. However, these clouds still produce rain, suggesting an overestimation of accretion. Lastly, the excessive rain production in thick clouds also point to an overly broad parameterized drop size distribution (DSD), which lead to an early initiation of autoconversion at cloud top and rain formation in clouds with large r_e.

Overall, in N=100 simulation (Figure 8), most modeled MBL clouds are optically thin ($\tau < 20$) and exhibit medium ($r_e = 10-15\ \mu m$, 49.8%) or large droplet sizes ($r_e = 15-20\ \mu m$, 25.8%). Compared to observations, model produces more clouds with larger drop size, while observations show a majority with $r_e < 10\ \mu m$ (53.3%; Figure 7, third column). Meanwhile, although the aerosol concentration is prescribed, the model predicts N_d through aerosol activation and microphysical processes, resulting in variabilities in N_d. For clouds with given optical depth, a decrease in r_e indicates an increase in N_d. This increase in N_d is associated with both lower peak of Z_e and a reduced vertical Z_e gradients in the CFODD, suggesting aerosol-induced precipitation suppression. Lastly, cloud dynamics plays a stronger role in the simulation than in observations. For example, thicker clouds in the model show higher peak Z_e values and broader Z_e distribution than thinner clouds with same r_e, whereas this enhancement is less evident in ARM observations.

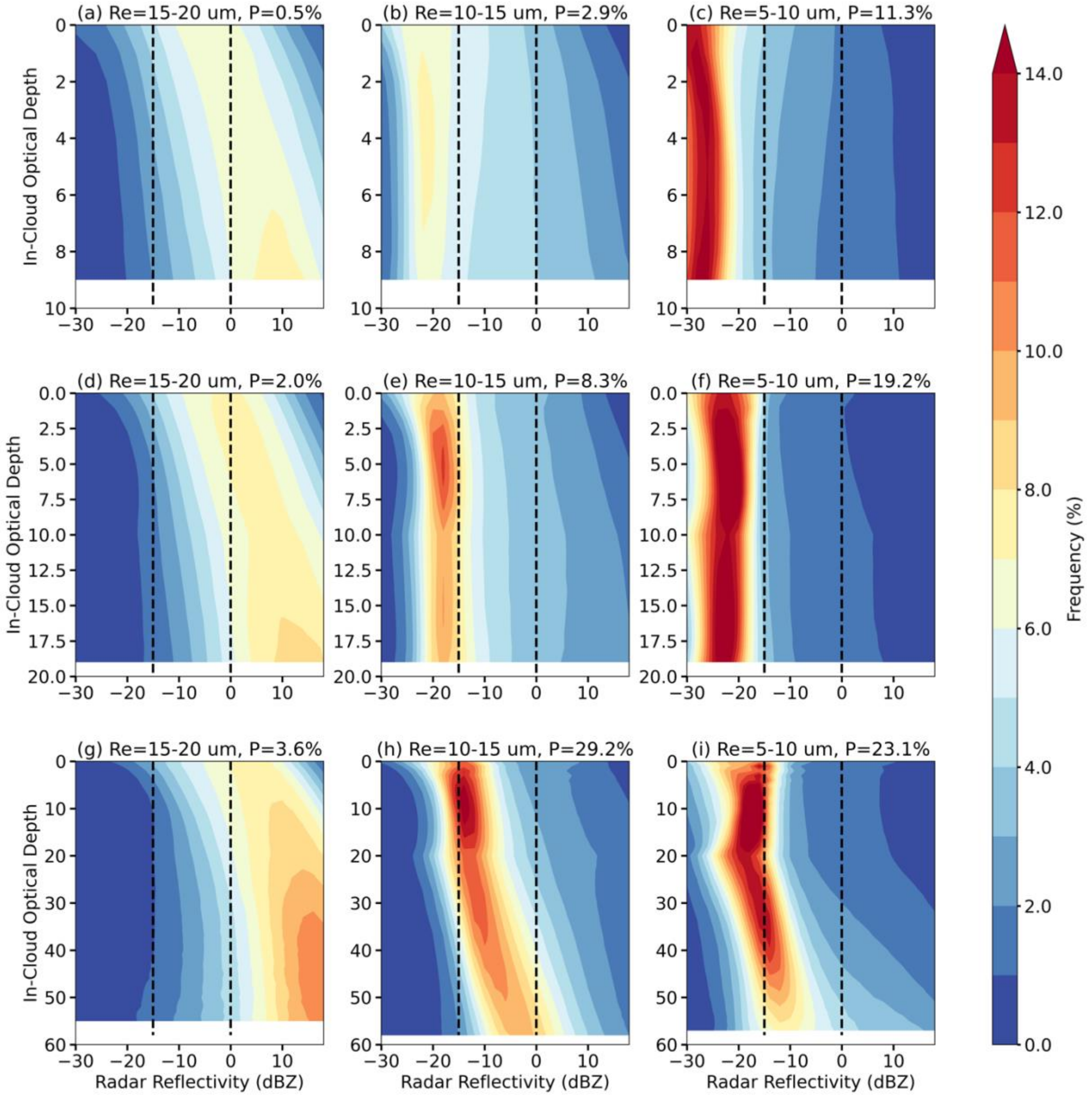

Figure 9. Frequency of radar reflectivity as a function of in-cloud optical depth (τ_d) for WRF N=500 simulation. Different rows are for different ranges of optical depth (τ): (a)-(c) clouds with $\tau < 10$, (d)-(f) clouds with $10 < \tau < 20$, (g)-(i) clouds with $\tau > 20$. Different columns are for different ranges of effective radius (r_e). The left, middle, and right columns are for $15-20\ \mu m$, $10-15\ \mu m$, and $5-10\ \mu m$, respectively. The black dashed lines in each panel denote -15 dBZ and 0 dBZ, as thresholds of drizzle and rain, respectively. The percentage of sample (P) for each subgroup is denoted in the figure.

Comparing simulations with different prescribed aerosol concentrations, we observe that with increasing aerosols and decreasing drop size, precipitation is suppressed. This is evidenced by the shift of frequency of occurrence of precipitating clouds, along with reduced peak Z_e and shallower gradient of Z_e. For example, the most common cloud type shifts from thin clouds with moderate r_e in the N=100 simulation (Figures 8b, e) to thicker clouds with smaller r_e in the N=500 run (Figures 9h, i), revealing a typical cloud response to precipitation suppression. Meanwhile, the percentage of clouds with $r_e = 15 - 20\ \mu m$ decreases significantly from 31.9% in N=100 to 6.1% in N=500 simulations. As a result, the droplet size distribution in N=500 simulation aligns better with ARM observations, although clouds are still thicker in model. For clouds with similar r_e and τ, both the peak Z_e and its vertical gradient decrease with increasing aerosol concentrations due to the reduced autoconversion with higher N_d. In particular, thick clouds with medium r_e ($r_e = 10 - 15\ \mu m, \tau >$20, Figure 9h) transition from raining to drizzling in the N=500 simulation, aligning more closely with observations.

For clouds with $r_e > 15\ \mu m$, rain becomes stronger compared to the N=100 simulation, even in the thinnest cloud (Figures 9 a, d, g vs. Figures 8 a, d, g). While the enhancement of precipitation with increasing aerosol concentration may initially seem counter-intuitive, it can be explained by the parameterization of DSD in the model. For clouds with similar τ, increasing r_e is associated with higher LWP and q_c, but lower N_d. Based on Equation (5), the slope parameter λ decreases with increasing r_e, resulting in a broader DSD with a flatter slope. Additionally, the dispersion parameter η is proportional to N_d so that polluted clouds in N=500 simulation also exhibit broader DSDs. As a result, even under suppressed autoconversion due to higher N_d, the extended tail of the broader DSD initiates autoconversion, enhances accretion from higher fall speed, and ultimately enhances precipitation in the N=500 simulation. Note that this type of cloud occurs much less frequently in the N=500 simulation (6.1%) than in the N=100 simulation (31.9%).

When continuously increasing aerosol concentration from N=500 to N=1000 (Figure 9 vs. Figure 10), the CFODD of reflectivity changes little, indicating a saturation of the precipitation suppression effect and the broadening of DSD. More clouds shift to the non-precipitating thick clouds subgroup with $r_e < 10\ \mu m$ and $\tau >$20 (44.6%, Figure 10i).

In summary, we evaluated the vertical development of precipitation in the model using ARM radar reflectivity profiles. Our simulations realistically reproduce the non-precipitating regime and the transition to drizzling clouds at similar r_e and τ ranges as ARM observations. Meanwhile, model overestimates precipitation for optically thick clouds and clouds with $r_e > 15\ \mu m$. This overestimation could be attributed to the early initiation of the autoconversion process, which leads to an early onset of rain near the cloud top. The excessive accretion rates, along with underestimation of entrainment and evaporation, lead to an overproduction of rain in the model, especially in thick clouds with larger water content and longer droplet collection path. Additionally, the parameterized DSD is too broad in the model, especially for polluted clouds with large N_d and large r_e.

As the model reasonably captures the properties of non-precipitating thin clouds in agreement with ARM observations, the simulated LWP susceptibility aligns well with satellite-based estimates. In contrast, the overestimation of precipitation in thick clouds leads to a predominantly positive LWP susceptibility in the model due to the precipitation suppression effect. However, satellite observations indicate that these clouds are typically non-precipitating, where entrainment drying dominates, resulting in a negative LWP susceptibility. This highlights the need to improve the parameterization of precipitation processes: particularly autoconversion, accretion, and DSD representation, in order to better simulate ACI across all cloud regimes.

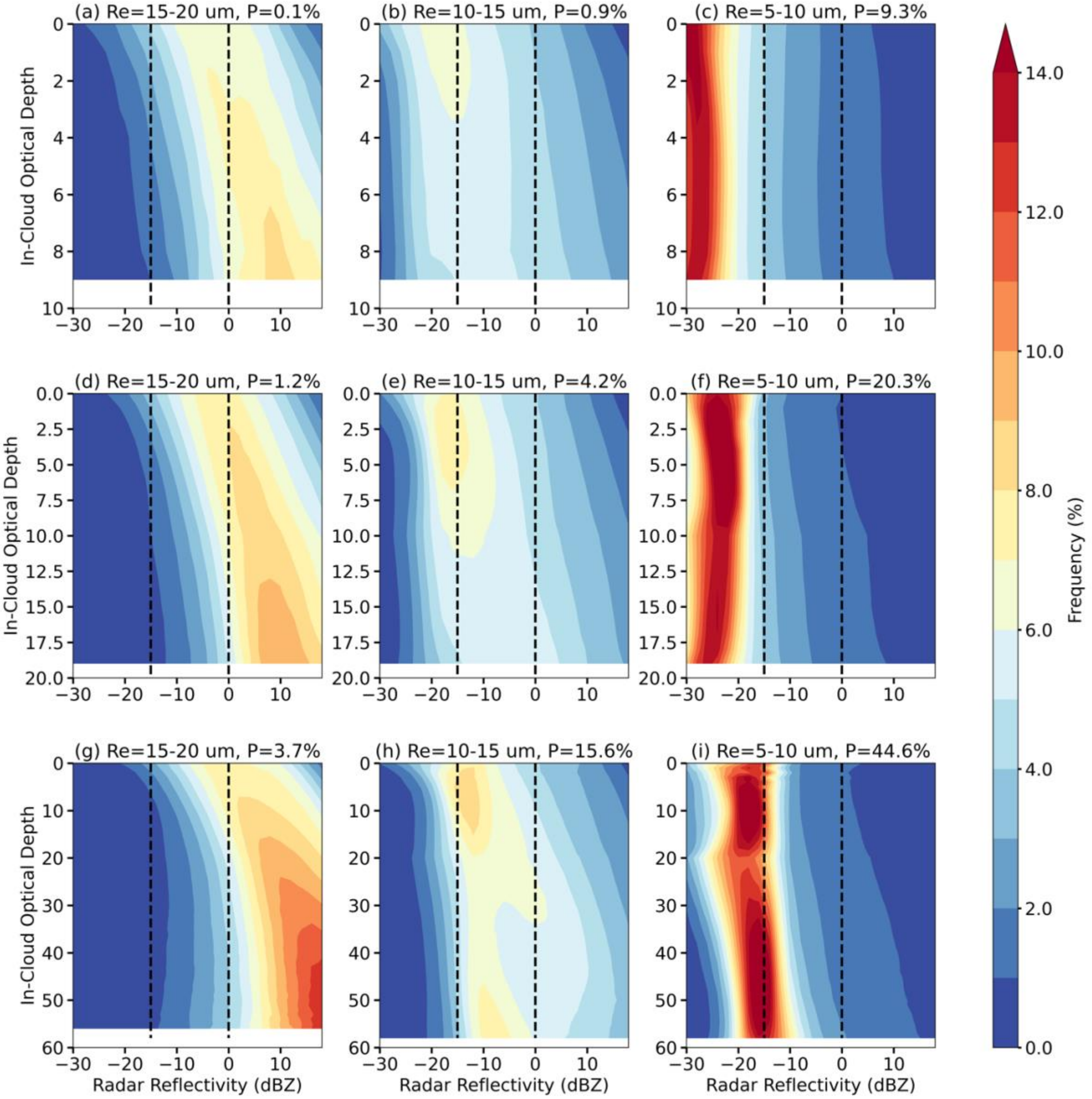

Figure 10. Frequency of radar reflectivity as a function of in-cloud optical depth (τ_d) for WRF N=1000 simulation. Different rows are for different ranges of optical depth (τ): (a)-(c) clouds with $\tau < 10$, (d)-(f) clouds with $10 < \tau < 20$, (g)-(i) clouds with $\tau > 20$. Different columns are for different ranges of effective radius (r_e). The left, middle, and right columns are for $15 - 20\ \mu m$, $10 - 15\ \mu m$, and $5 - 10\ \mu m$, respectively. The black dashed lines in each panel denote -15 dBZ and 0 dBZ, as thresholds of drizzle and rain, respectively. The percentage of sample (P) for each subgroup is denoted in the figure.

While our analysis focuses on the two-moment Morrison scheme, Christensen et al. (2024) found that the choice of microphysics and PBL schemes accounts for only about 30 % of the variability in simulated ACI, much smaller than the variability across meteorological conditions and cloud states. Since this study encompasses 11 cases spanning diverse synoptic regimes and cloud types, the overall conclusions are unlikely to change substantially with alternative two-moment bulk microphysics schemes. Nonetheless, future investigations using multiple microphysics schemes would be valuable for quantifying the robustness of the precipitation parameterization and its role in ACI uncertainty.

3.3.2 Model Bias in Capturing Inversions

As discussed in case study in Section 3.1, ERA5 profiles fail to accurately represent the location and strength of inversions over the ENA region. These biases lead to an underestimated boundary layer height and an overestimated RH above cloud top in the simulations. Figure 11 compares the probability density function (PDF) of cloud-top RH between ARM sounding observations and WRF simulations across all 11 cases for N=1000 simulation. Different aerosol concentrations (e.g., N=100, N=500) show consistent results (not shown). In ARM observations, cloud-top height is derived from the radar reflectivity profile, as described in the method section; while in WRF simulations, cloud top is defined as the highest model level where the cloud water mixing ratio exceeds 0.001 g/kg. The RH is sampled at ~100m above cloud top in both data. We further compare the cloud-top heights in WRF simulations defined using cloud water mixing ratio and radar reflectivity profiles with Z_e > -40 dBZ from the radar simulator. The two approaches yield nearly identical results, with a mean difference of less than 40m (figure not shown).

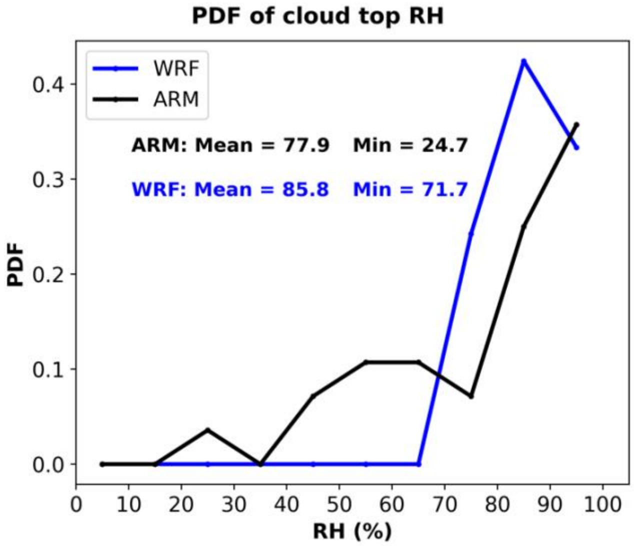

Figure 11. PDF of cloud top relative humidity (RH) for WRF simulations (blue line) and ARM sounding observations (black line).

To ensure a meaningful comparison between WRF output and ground-based observations, cloud-top RH from WRF is averaged over a 10km × 10km grid box centered at the ARM ENA site for each sounding time, given the ~1.2-1.4 km mean cloud-top height for MBL clouds and ~7 m/s prevailing wind speed at ENA during summer (Wood et al., 2015; Wu et al., 2020). As seen in Figure 11, WRF simulations exhibit a systematic wet bias in cloud-top RH, with the mean values 7.9% higher than those from observations and with no RH values below 71%.

Figure 12 shows the mean relationship between clout top RH and cloud susceptibilities calculated based on domain mean values for all three simulations (e.g. N=1000 vs. N=100, N=500 vs. N=100, and N=1000 vs. N=500). The cloud top RH is the domain mean RH value at ~100m above cloud top for all simulations. As seen in Figure 12a, we find a positive correlation between cloud-top RH and LWP susceptibility in the simulations, which is consistent with cloud responses shown in case study where a dry layer above cloud promotes evaporation and decrease LWP. Additionally, these positive relationships are consistent among different aerosol concentrations (e.g., N=1000 vs. N=100 or N=500 vs. N=100; figures not shown). Meanwhile, as seen in Figure 12, cloud top moisture has a more evident impact on cloud LWP than cloud cover. Relations between cloud top moisture and cloud susceptibilities found in our simulations are consistent with that in satellite observations around the globe (e.g. Toll et al., 2019; Yuan et al., 2023), except that LWP susceptibility is mostly negative while CF susceptibility is mostly positive in satellite data.

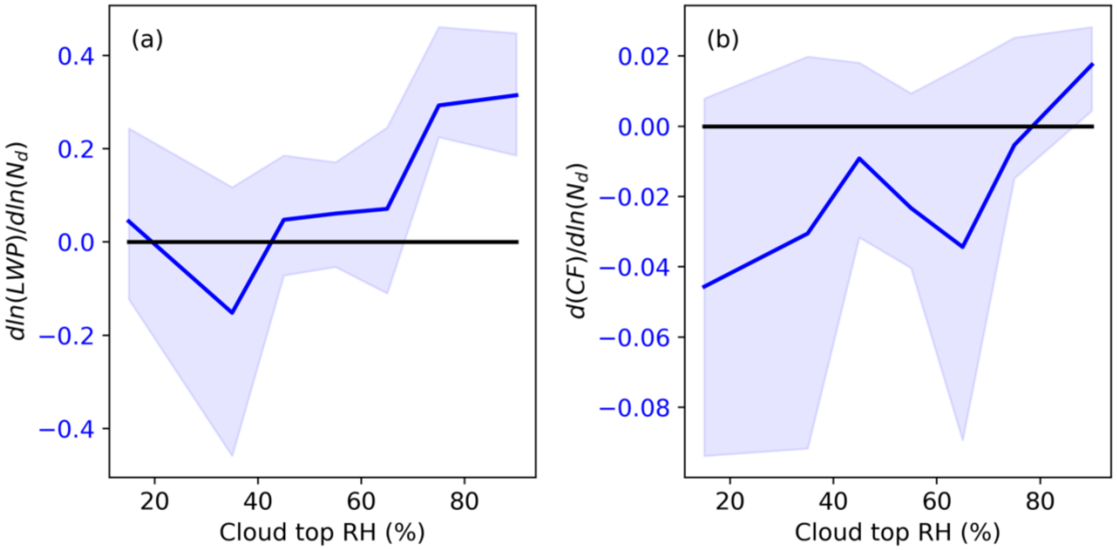

Figure 12. Dependence of (a) LWP susceptibility and (b) CF susceptibility on cloud top relative humidity in WRF simulations during the daytime. The solid blue line shows the median value of each RH bins and the shaded area shows the lower and upper 25th percentiles.

Based on the relationship between cloud susceptibility and cloud-top RH, the over-estimated cloud-top RH of 8% may lead to an overestimation of 0.04 and 0.005 in LWP and CF susceptibility, respectively. Meanwhile, the under-estimated cloud-top height of 480m could result in an under-estimation of LWP and CF susceptibility of 0.18 and 0.02, respectively (figures not shown). Future modeling studies over the ENA region need to improve the initial and boundary conditions, e.g., through data assimilations.

To further illustrate the influence of cloud-top evaporation on LWP and CF adjustment rate, we analyzed the relationship between cloud susceptibilities and change in the cloud-layer buoyancy flux. As shown in the case study, buoyancy flux increases with aerosol perturbation in precipitating clouds due to precipitation suppression, whereas it decreases in non-precipitating clouds due to enhanced entrainment driven evaporation. Thus, changes in buoyancy flux serves as a proxy for both cloud-top evaporation and precipitation suppression effects.

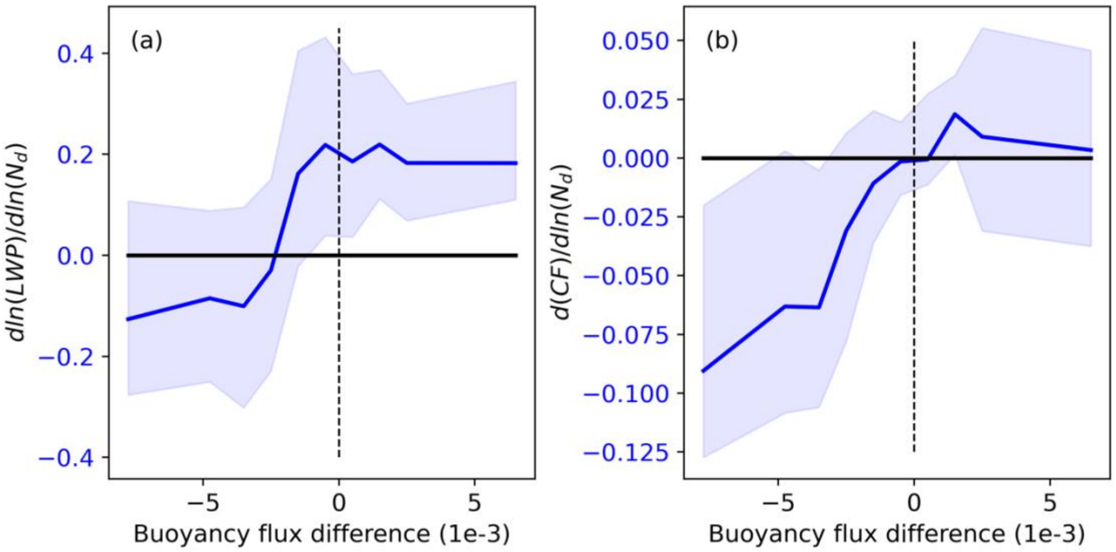

Figure 13. Dependence of (a) LWP susceptibility and (b) CF susceptibility on changes in buoyancy flux in the cloud layer in WRF simulations during the daytime. The solid blue line shows the median value of each buoyancy flux bins and the shaded area shows the lower and upper 25th percentiles.

In Figure 13, changes in cloud-layer buoyancy flux is calculated as the difference in domain-mean values between polluted and clean experiments (e.g., N=1000 vs. N=100, N=500 vs. N=100, and N=1000 vs. N=500), averaged in the cloud layer defined by the domain-mean cloud water mixing ratio. As shown in Figure 13, two distinct regimes emerge: when cloud-layer buoyancy flux substantially decrease with increasing aerosols, both LWP and CF decrease; when changes in buoyancy flux is small negative or positive, LWP and CF susceptibilities are generally positive or near zero. These results, together with those in Figure 12, support the conclusion that the reduction in LWP and CF in the model is primarily driven by cloud-top evaporation associated with enhanced entrainment. The absence of negative LWP responses in earlier modeling studies may be attributed to inadequate resolution of the interactions among boundary layer turbulence, entrainment, and cloud-top evaporation.

3.3.3 LWP Adjustment from Internal Cloud Processes and Precipitation Heterogeneity

In addition to model biases in representing precipitation processes and PBL thermodynamic profiles, one leading factor contributing to the discrepancy in ACI estimates lies in how ACI is diagnosed in numerical studies versus observations. In model simulations, ACI can be isolated using controlled experiments by varying aerosol concentrations while holding meteorology constant. In satellite-based analysis, however, the retrieved ACI signal inevitably includes not only aerosol-induced cloud responses but also N_d–LWP covariability arising from internal cloud processes, even under strict spatial and temporal sampling constraints. Diagnosing these internal cloud processes in satellite observations is difficult because key governing variables, such as cloud-base updraft speed, TKE, entrainment rate are not directly measured or retrieved. In contrast, model simulations allow us to quantify the N_d–LWP relationships driven by internal cloud processes by examining their spatial covariation under homogeneous aerosol conditions.

To ensure consistency with satellite methodology and suppress small-scale cloud heterogeneity, pixel-level model outputs are aggregated to a 25 km × 25 km grid.

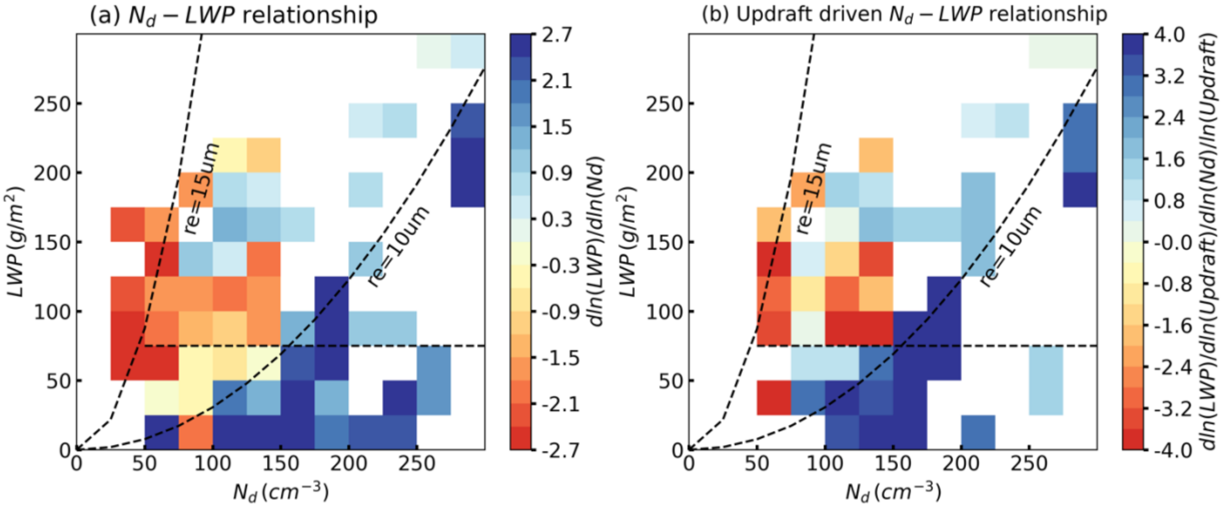

Figure 14. (a) LWP-N_d relations stem from internal cloud processes (b) LWP-N_d relations driven by cloud base updraft speed in WRF simulations during the daytime.

Figure 14a shows the resulting N_d–LWP relationships across all cases and all aerosol concentrations, revealing opposing signs between different cloud regimes: a strong positive correlation for non-precipitating clouds and a strong negative correlation for precipitating clouds. To understand this contrast, we examine whether both N_d and LWP co-vary with a third parameter indicative of internal dynamics. Cloud-base updraft speed emerges as a physical meaningful driver: the ratio of $\frac{dln(LWP)}{dln(Updraft)}$ to $\frac{dln(N_d)}{dln(Updraft)}$ in Figure 14b closely mirrors the N_d–LWP relations in Figure 14a. This indicates that cloud base updraft speed largely governs the opposing responses. In non-precipitating clouds, stronger updrafts enhance supersaturation, activation, and condensation, increasing both N_d and LWP, and resulting in a positive N_d–LWP relationship. In precipitating clouds, stronger updrafts increase LWP and rain rate, but precipitation formation reduces N_d via coalescence and collection, leading to a negative relation.

Furthermore, mesoscale variability in precipitation structure can further modulate the N_d–LWP relationship in precipitating clouds. To test this hypothesis, precipitating cases (domain-mean precipitation fraction > 0.1) are further divided into heterogeneous and homogeneous categories based on the spatial standard deviation of precipitation fraction using the upper and lower 50th percentile, respectively (Figure 15). Precipitation fraction is defined as the areal fraction of cloud pixels with the column maximum reflectivity greater than –15 dBZ (Figure 6).

In heterogeneous convective precipitation (Figure 15a), strong and spatially variable latent heating release enhances buoyancy within clouds, while rain evaporation and downdrafts generate cold pools. Both processes act to intensify updrafts, which in turn promote rapid droplet growth and increase the cloud's capacity to retain liquid water, leading to higher LWP and precipitation. Meanwhile, stronger coalescence and precipitation scavenging reduce N_d. Such opposite changes in LWP and N_d amplify the negative N_d–LWP relationship (Figure 15c). In homogeneous stratiform precipitation, latent heating is more spatially uniform and stratification inhibits localized buoyancy-driven updrafts. Weaker coalescence and less efficient scavenging lead to a less negative N_d–LWP relationship (Figure 15d).

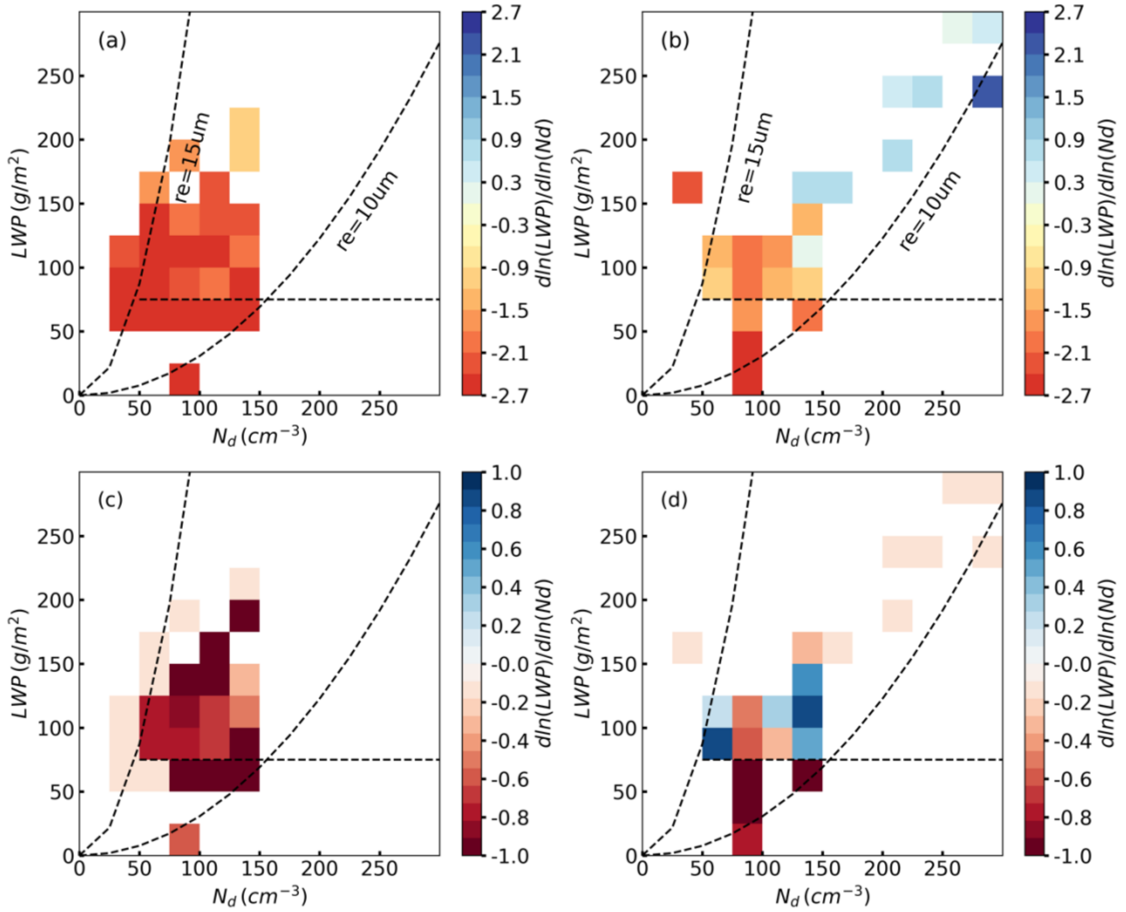

Figure 15. Same as Figure 14, but for scenes with (a) heterogeneous and (b) homogeneous precipitation fraction. (c) and (d) show the difference between (a) and (b) with Figure 14a.

In summary, even though clouds with LWP > 75 g/m² and $r_e < 15$ µm are typically classified as non-precipitating thick clouds in observational ACI studies, pixel-level data real that 20–35% of these clouds produce precipitation (Figure 6a). The strongly negative LWP susceptibilities inferred from satellite data for non-precipitating thick clouds may partly arise from internal cloud processes driven by updraft speed and mesoscale precipitation structure, rather than from aerosol–cloud interactions alone. providing a plausible explanation for the model–observation discrepancy. Meanwhile, non-precipitating thin clouds with LWP < 75 g/m² and $r_e < 15$ µm exhibit low pixel-level precipitation fractions (typically < 0.1, Figure 6a), and the positive N_d–LWP relationships arising from internal cloud processes may bias satellite-derived LWP susceptibility toward more positive values, further expanding the model-observation gap. The opposing signs of N_d–LWP relationships in Figures 14a and 5c for non-precipitating thin clouds highlight the need for additional process-level analysis in future study.

4. Conclusions and Discussions

Previous studies found that model simulations and observations often reveal opposing results in LWP responses to aerosol perturbations for MBL clouds. For example, satellite-based assessments indicate a decrease of cloud LWP with aerosol perturbations, especially in polluted conditions for non-precipitating clouds (e.g., Gryspeerdt et al. 2019; Toll et al., 2019; Zhang et al., 2022, 2023; Qiu et al., 2024; Yuan et al., 2023; 2025). On the other hand, most GCMs and CPMs simulate an increase of LWP with increasing aerosols (e.g., Ghan et al., 2016; Michibata et al., 2016; Mülmenstädt et al., 2024; Fons et al., 2024; Christensen et al, 2024). Previous studies found that increasing model resolution to sub-kilometer can improve the representation of precipitation process and model performance in ACI by resolving the small-scale process most relevant to ACI (e.g., Terai et al., 2020). It remains unclear how well models perform at close to LES scale in representing the ACI feedback when using realistic meteorological conditions and large case ensembles across various cloud states and synoptic regimes.

To address these gaps, our study makes three key advances: (1) we conduct a series of realistic near-LES-scale case studies that enable direct comparison with ground-based and satellite observations to reconcile observed–modeled discrepancies; (2) we examine a large ensemble of MBL cloud cases spanning a range of cloud states and synoptic conditions to capture the diversity of ACI responses; and (3) we use the same two-moment microphysics scheme implemented in several GCMs and CPMs, making our findings directly relevant for improving microphysical parameterizations in climate models.

The simulated MBL clouds generally match the satellite observation in domain mean cloud coverage and mesoscale organization (Figures 1, 3, S2-S4), while the model may struggle to capture the diurnal evolution of clouds, especially the dissipation of clouds in the afternoon. Model overestimate cloud LWP, especially in the polluted runs and underestimated cloud top height compared to satellite retrievals. To show the dependence of cloud responses on cloud state, LWP susceptibilities are displayed in the N_d-LWP parameter space (Figure 5). For non-precipitating thin clouds, our simulations show a consistently negative but weaker LWP susceptibility compared to satellite observations, with a mean of-0.13. The negative LWP susceptibility likely result from the better resolved turbulence, condensation/evaporation processes and their feedback on PBL thermodynamics. More specifically, increases in aerosols enhance turbulence and TKE in the cloud layer. With the dry air above, the entrained dry air intensifies evaporation, reduces buoyancy flux in the cloud layer and leads to dissipations of clouds (Figure 4, 13).

For precipitating clouds, our model predicts a slight increase in LWP with the mean susceptibility of $+0.15$, which is consistent with the precipitation suppression hypothesis and the climatological mean cloud response for heavily precipitating clouds (e.g., Qiu et al., 2024). For non-precipitating thick clouds, model simulations and satellite observations show the largest disagreement with opposite LWP susceptibilities of $+0.32$ vs. -0.69, respectively. Meanwhile, the non-precipitating thick clouds are the dominant cloud state in the model, with a total frequency of 49%, compared to a 15.7% frequency of occurrence in satellite observations. The overestimation of N_d arise from the overestimated aerosol concentration in the configuration, combined with the absence of precipitation scavenging in the model. The overestimation of LWP is due to the positive LWP susceptibility in thick clouds where LWP in N=100 simulation show good agreement with satellite retrievals (Figure S9)

Our analyses indicate that such discrepancy could mainly result from the overestimation of precipitation for thick clouds: where MBL clouds in simulations produce precipitation at much smaller cloud drop size (e.g., $r_e > 10\ \mu m$) and in more polluted conditions compared to satellite observations (Figure 6). Based on ARM radar observations, our simulations reasonably capture the non-precipitating regime and the transition from non-precipitating to drizzling clouds within the same r_e and τ range as observed (Figures 7, 8). Our simulation result appears to better represent marine clouds than GCM or GCPM, which often initiate drizzle or rain at cloud top and rarely simulate non-precipitating clouds (e.g., Jing et al. 2017, 2019; Michibata and Suzuki, 2020). However, several biases remain. In non-precipitating clouds, the model shows near-constant Z_e profile with height, whereas observations show a decrease near cloud top, suggesting an underestimation of entrainment and evaporation (Figure 8). In thicker clouds ($\tau > 20$), drizzle often initiates too early at cloud top ($Z_e > -15$ dBZ), indicating excessive autoconversion. This early onset allows raindrops to grow too large through prolonged collection in deeper clouds, resulting in overestimated rain rates ($Z_e > 0$ dBZ), whereas observations show only drizzle (Figure 8). Additionally, stronger rain in polluted cases with large r_e points to an overly broad DSD, as the dispersion parameter η in the Morrison scheme increases with N_d, and the DSD slope flattens with larger r_e (Figures 9, 10). The overestimation of precipitation for thick clouds results in an increase in LWP from precipitation suppression in the simulation.

The overestimation of LWP susceptibility may also stem from biases in ERA5 and WRF profiles in representing the location and strength of moisture inversions (Figures S6, S8), leading to shallower PBL and a moist bias above the clouds in the simulations (Figure 11). Consistent with observations, model simulations show a positive correlation between LWP susceptibility and cloud-top RH, suggesting that the wet bias in cloud-top RH contributes to the positive bias in LWP susceptibility (Figure 12).

Lastly, we find that part of the discrepancy in quantified ACI may stem from N_d-LWP relationships driven by internal cloud processes that are mixed with the ACI signals in satellite observations. Using model simulations with homogenous aerosol concentrations, we isolate these internally driven N_d-LWP relationships. Our results reveal large opposing signals between precipitating clouds (large negative relationships) and non-precipitating clouds (large positive relationships), primarily governed by cloud base updraft speed (Figures 14) and modulated by mesoscale cloud and precipitation organization (Figure 15). Therefore, the strongly negative LWP susceptibility observed in thick clouds in satellite data could reflect internal cloud dynamics rather than true ACI.

This study shows that while the discrepancy in ACI assessments between observations and models can be reduced by increasing model resolution for precipitating and non-precipitation thin clouds, the positive bias in the LWP susceptibility for non-precipitating thick clouds persists. This bias is attributed to parameterization deficiencies in the microphysics scheme and model biases in lower tropospheric thermodynamics over the ENA region. These findings may motivate improvements in precipitation parameterizations and encourage their process-level evaluation against observations.

Data availability:

The WRF model used, version 4.2.2, is freely available from the developers' website (https://github.com/wrf-model/WRF/releases, WRF, 2022). SEVIRI Meteosat cloud retrieval products, produced by NASA LaRC SatCORPS group, are available from the Atmospheric Radiation Measurement (ARM) Data Discovery website at https://adc.arm.gov/discovery/, Minnis Cloud Products Using Visst Algorithm. The ARM ground-based radar and lidar observations (KAZRARSCL), LWP retrievals, and balloon sounding observations are available from ARM Data Discovery.

Acknowledgments:

We are grateful to the Atmospheric Radiation Measurement (ARM) user facility, a U.S. Department of Energy (DOE) Office of Science user facility managed by the Biological and Environmental Research Program for providing ARM observation data and archiving SEVIRI Meteosat cloud retrieval products. We mainly used the computing resources from the National Energy Research Scientific Computing Center (NERSC), which is supported by the Office of Science of the U.S. Department of Energy under Contract No. DE-AC02-05CH11231. This work was performed under the auspices of the U.S. DOE by LLNL under contract DE-AC52-07NA27344. LLNL-JRNL-2008226. PNNL is operated by Battelle for the U.S. Department of Energy under Contract DE-AC05-76RLO1830. Xiaoli Zhou acknowledges the funding support from the Canada First Research Excellence Fund Transforming Climate Action program (TCA-LRP-20241-1.1-05).

Author contribution:

SQ carried out the data analysis and wrote the manuscript. XZ and HL ran the simulations. PW provided the ground-based cloud microphysics retrievals. All authors contributed to the design of the study, interpretation of the results, and edit the manuscript.

Financial support:

This work is supported by the DOE Office of Science Early Career Research Program and the ASR Program.

Competing interests:

The authors declare that they have no conflict of interest.

References

Ackerman A, Kirkpatrick M, Stevens D, Toon O (2004). The impact of humidity above stratiform clouds on indirect aerosol climate forcing. Nature; 432(7020):1014–7. https://doi.org/10.103 8/nature03174.

Albrecht, B. A.: Aerosols, Cloud Microphysics, and Fractional Cloudiness, Science, 245, 1227–1230, https://doi.org/10.1126/science.245.4923.1227, 1989.

Arola, A., Lipponen, A., Kolmonen, P., Virtanen, T. H., Bellouin, N., Grosvenor, D. P., Gryspeerdt, E., Quaas, J., & Kokkola, H. (2022). Aerosol effects on clouds are concealed by natural cloud heterogeneity and satellite retrieval errors. Nature Communica)ons, 13(1), 7357. hrps://doi.org/10.1038/s41467-022-34948-5Bennartz, R.: Global assessment of marine boundary layer cloud droplet number concentration from satellite, J. Geophys. Res.,112, D02201, doi:10.1029/2006JD007547, 2007.

Abdul-Razzak, H., & Ghan, S. J. (2000). A parameterization of aerosol activation: 2. Multiple aerosol types. Journal of Geophysical Research: Atmospheres, 105(D5), 6837-6844. https://doi.org/https://doi.org/10.1029/1999JD901161

Bretherton CS, Blossey PN, Uchida J. Cloud droplet sedimentation, entrainment efficiency, and subtropical stratocumulus albedo. Geophys Res Lett. 2007; 34(3). https://doi.org/10.1029/2006GL027648.

Cadeddu, M. P., Liljegren, J. C., & Turner, D. D. (2013). The atmospheric radiation measurement (ARM) program network of microwave radiometers: Instrumentation, data, and retrievals. Atmospheric Measurement Techniques, 6(9), 2359–2372. https://doi.org/10.5194/amt-6-2359-2013

Caldwell, P. M., Terai, C. R., Hillman, B., Keen, N. D., Bogenschutz, P., Lin, W., et al. (2021). Convection-permitting simulations with the E3SM global atmosphere model. Journal of Advances in Modeling Earth Systems, 13, e2021MS002544. https://doi.org/10.1029/2021MS002544

Chen, Y., Haywood, J., Wang, Y., Malavelle, F., Jordan, G., Partridge, D., Fieldsend, J., De Leeuw, J., Schmidt, A., Cho, N., Oreopoulos, L., Platnick, S., Grosvenor, D., Field, P., & Lohmann, U. (2022): Machine learning reveals climate forcing from aerosols is dominated by increased cloud cover. *Nature Geoscience*, *15*(8), 609-614, https://doi.org/10.1038/s41561-022-00991-6

Chen, Y. S., Zhang, J., Hoffmann, F., Yamaguchi, T., Glassmeier, F., Zhou, X., & Feingold, G. (2024). Diurnal evolution of non-precipitating marine stratocumuli in a large-eddy simulation ensemble. Atmospheric Chemistry and Physics, 24(22), 12661-12685.

Christensen, M. W., Wu, P., Varble, A. C., Xiao, H., and Fast, J. D.: Aerosol-induced closure of marine cloud cells: enhanced effects in the presence of precipitation, Atmos. Chem. Phys., 24, 6455-6476, 10.5194/acp-24-6455-2024, 2024.

Clothiaux, E. E., Miller, M. A., Perez, R. C., Turner, D. D., Moran, K. P., Martner, B. E., Ackerman, T. P., Mace, G. G., Marchand, R. T., Widener, K. B., Rodriguez, D. J., Uttal, T., Mather, J. H., Flynn, C. J., Gaustad, K. L., & Ermold, B. (2001). The ARM Millimeter Wave Cloud Radars (MMCRs) and the Active Remote Sensing of Clouds (ARSCL) Value Added Product (VAP). https://www.osti.gov/biblio/1808567, https://www.osti.gov/servlets/purl/1808567

Donahue, A. S., Caldwell, P. M., Bertagna, L., Beydoun, H., Bogenschutz, P. A., Bradley, A. M., et al. (2024). To exascale and beyond—The Simple Cloud-Resolving E3SM Atmosphere Model (SCREAM), a performance portable global atmosphere model for cloud-resolving scales. *Journal of Advances in Modeling Earth Systems*, 16, e2024MS004314. https://doi.org/10.1029/2024MS004314

Dong, X., Ackerman, T. P., Clothiaux, E. E., Pilewskie, P., & Han, Y. (1997). Microphysical and radiative properties of boundary layer stratiform clouds deduced from ground-based measurements. *Journal of Geophysical Research: Atmospheres*, *102*(D20), 23829-23843.

Dong, X., Ackerman, T. P., & Clothiaux, E. E. (1998). Parameterizations of the microphysical and shortwave radiative properties of boundary layer stratus from ground-based measurements. *Journal of Geophysical Research: Atmospheres*, *103*(D24), 31681-31693.

Dong, X., Mace, G. G., Minnis, P., Smith Jr, W. L., Poellot, M., Marchand, R. T., & Rapp, A. D. (2002). Comparison of stratus cloud properties deduced from surface, GOES, and aircraft data during the March 2000 ARM Cloud IOP. *Journal of the Atmospheric Sciences*, *59*(23), 3265-3284.

Dong, X., Xi, B., Kennedy, A., Minnis, P., & Wood, R. (2014). A 19-month record of marine aerosol–cloud–radiation properties derived from DOE ARM mobile facility deployment at the Azores. Part I: Cloud fraction and single-layered MBL cloud properties. Journal of Climate, 27(10), 3665–3682. https://doi.org/10.1175/JCLI-D-13-00553.1.

Dong, X., Zheng, X., Xi, B., & Xie, S. (2023). A Climatology of Midlatitude Maritime Cloud Fraction and Radiative Effect. Derived from the ARM ENA Ground-Based Observations. Journal of Climate, 36(2), 531–546, https://doi.org/10.1175/JCLI-D-22-0290.1.

Fons, E., Naumann, A. K., Neubauer, D., Lang, T., & Lohmann, U. (2024). Investigating the sign of stratocumulus adjustments to aerosols in the global storm-resolving model ICON. *EGUsphere*, *2024*, 1-30.

Forster, P., T. Storelvmo, K. Armour, W. Collins, J.-L. Dufresne, D. Frame, D.J. Lunt, T. Mauritsen, M.D. Palmer, M. Watanabe, M. Wild, and H. Zhang, 2021: The Earth's Energy Budget, Climate Feedbacks, and Climate Sensitivity. In Climate Change (2021). The Physical Science Basis. Contribution of Working Group I to the Sixth Assessment Report of the Intergovernmental Panel on Climate Change. Cambridge University Press, Cambridge, United Kingdom and New York, NY, USA, pp. 923–1054, doi: 10.1017/9781009157896.009.

Golaz, J.-C., Van Roekel, L. P., Zheng, X., Roberts, A. F., Wolfe, J. D., Lin, W., et al. (2022). The DOE E3SM Model version 2: Overview of the physical model and initial model evaluation. Journal of Advances in Modeling Earth Systems, 14, e2022MS003156. https://doi.org/10.1029/2022MS003156

Ghan S, Wang M, Zhang S, Ferrachat S, Gettelman A, Griesfeller J, Kipling Z, Lohmann U, Morrison H, Neubauer D, Partridge DG, Stier P, Takemura T, Wang H, Zhang K. Challenges in constraining anthropogenic aerosol effects on cloud radiative forcing using present-day spatiotemporal variability. Proc Natl Acad Sci USA. 2016;113(21):5804–11.https://doi.org/10.1073/pnas.1514036113.

Ghate, V. P., Surleta, T., Magaritz-Ronen, L., Raveh-Rubin, S., Gallo, F., Carlton, A. G., & Azevedo, E. B. (2023). Drivers of cloud condensation nuclei in the Eastern North Atlantic as observed at the ARM site. Journal of Geophysical Research: Atmospheres, 128, e2023JD038636. https://doi.org/10.1029/2023JD038636

Ghate, V. P., Cadeddu, M. P., Zheng, X., & O'Connor, E. (2021). Turbulence in the marine boundary layer and air motions below stratocumulus clouds at the ARM eastern North Atlantic Site. Journal of Applied Meteorology and Climatology, 60(10), 1495–1510. https://doi.org/10.1175/jamc-d-21-0087.1

Glassmeier, F., Hoffmann, F., Johnson, J. S., Yamaguchi, T., Carslaw, K. S., and Feingold, G.: An emulator approach to stratocumulus susceptibility, Atmos. Chem. Phys., 19, 10191–10203, https://doi.org/10.5194/acp-19-10191-2019, 2019.

Grosvenor, D. P., Sourdeval, O., Zuidema, P., Ackerman, A., Alexandrov, M. D., Bennartz, R., Boers, R., Cairns, B., Chiu, J. C., Christensen, M., Deneke, H., Diamond, M., Feingold, G., Fridlind, A., HÃOEnerbein, A., Knist, C., Kollias, P., Marshak, A., McCoy, D., Merk, D., Painemal, D., Rausch, J., Rosenfeld, D., Russchenberg, H., Seifert, P., Sinclair, K., Stier, P., van Diedenhoven, B., Wendisch, M., Werner, F., Wood, R., Zhang, Z., and Quaas, J.: Remote Sensing of Droplet Number Concentration in Warm Clouds: A Review of the Current State of Knowledge and Perspectives, Rev. Geophys., 56, 409–453, https://doi.org/10.1029/2017RG000593, 2018.

Gryspeerdt, E., Goren, T., Sourdeval, O., Quaas, J., Mülmenstädt, J., Dipu, S., Unglaub, C., Gettelman, A., and Christensen, M.: Constraining the aerosol influence on cloud liquid water path, Atmos. Chem. Phys., 19, 5331-5347, 10.5194/acp-19-5331-2019, 2019.

Gryspeerdt, E., Goren, T., and Smith, T. W. P.: Observing the timescales of aerosol–cloud interactions in snapshot satellite images, Atmos. Chem. Phys., 21, 6093–6109, https://doi.org/10.5194/acp-21-6093-2021, 2021.

Han, Q., Rossow, W. B., Zeng, J., and Welch, R.: Three Different Behaviors of Liquid Water Path of Water Clouds in Aerosol–Cloud Interactions, J. Atmos. Sci., 59, 726–735, https://doi.org/10.1175/1520-0469(2002)059<0726:TDBOLW>2.0.CO;2, 2002.

Haynes, J. M., L'Ecuyer, T. S., Stephens, G. L., Miller, S. D., Mitrescu, C., Wood, N. B., & Tanelli, S. (2009). Rainfall retrieval over the ocean with spaceborne W-band radar. Journal of Geophysical Research: Atmospheres, 114(D8).

Hoffmann, F., Glassmeier, F., Yamaguchi, T., and Feingold, G.: Liquid water path steady states in stratocumulus: Insights from process-level emulation and mixed-layer theory, J. Atmos. Sci.,77, 2203–2215, https://doi.org/10.1175/JAS-D-19-0241.1, 2020.

Jing, X., Suzuki, K., Guo, H., Goto, D., Ogura, T., Koshiro, T., & Mülmenstädt, J. (2017). A multimodel study on warm precipitation biases in global models compared to satellite observations. Journal of Geophysical Research: Atmospheres, 122, 11,806–11,824. https://doi.org/10.1002/2017JD027310.

Jing, X., Suzuki, K., & Michibata, T. (2019). The key role of warm rain parameterization in determining the aerosol indirect effect in a global climate model. *Journal of Climate*, *32*(14), 4409-4430.

Kaufman, Y. J., Koren, I., Remer, L. A., Rosenfeld, D., & Rudich, Y.: The effect of smoke, dust, and pollution aerosol on shallow cloud development over the Atlantic Ocean. *Proc Natl Acad Sci U S A*, *102*(32), 11207-11212. https://doi.org/10.1073/pnas.0505191102, 2005

Kokkola, H., Tonttila, J., Calderón, S.M., Romakkaniemi, S., Lipponen, A., Peräkorpi, A., Mielonen, T., Gryspeerdt, E., Virtanen, T.H., Kolmonen, P. and Arola, A., 2025. Model analysis of biases in the satellite-diagnosed aerosol effect on the cloud liquid water path. *Atmospheric Chemistry and Physics*, *25*(3), pp.1533-1543.

Lee, H. H., Zheng, X., Qiu, S., & Wang, Y. (2025). Numerical case study of the aerosol–cloud interactions in warm boundary layer clouds over the eastern North Atlantic with an interactive chemistry module. Atmospheric Chemistry and Physics, 25(12), 6069-6091.

Li, W., Li, L., Fu, R., Deng, Y., & Wang, H. (2011). Changes to the North Atlantic subtropical high and its role in the intensification of summer rainfall variability in the southeastern United States. Journal of Climate, 24(5), 1499-1506.

Mechem, D. B., Wittman, C. S., Miller, M. A., Yuter, S. E., and De Szoeke, S. P.: Joint synoptic and cloud variability over the Northeast Atlantic near the Azores, J. Appl. Meteorol. Clim., 57, 1273–1290, 2018.

Mellor, G. L. and Yamada, T.: Development of a turbulence closure model for geophysical fluid problems, Reviews of Geophysics, 20, 851-875, https://doi.org/10.1029/RG020i004p00851, 1982.

Mlawer, E. J., Taubman, S. J., Brown, P. D., Iacono, M. J., and Clough, S. A.: Radiative transfer for inhomogeneous atmospheres: RRTM, a validated correlated-k model for the longwave, Journal of Geophysical Research: Atmospheres, 102, 16663-16682, https://doi.org/10.1029/97JD00237, 1997.

Michibata T, Suzuki K, Sato Y, Takemura T (2016). The source of discrepancies in aerosol-cloud-precipitation interactions between GCM and A-Train retrievals. Atmos Chem Phys., 16(23):15,413–24. https://doi.org/10.5194/acp-16-15413-2016.

Michibata, T., & Suzuki, K. (2020). Reconciling compensating errors between precipitation constraints and the energy budget in a climate model. *Geophysical Research Letters*, *47*(12), e2020GL088340

Minnis, P., Sun-Mack, S., Chen, Y., Chang, F.-L., Yost, C. R., Smith, W. L., Heck, P. W., Arduini, R. F., Bedka, S. T., Yi, Y., Hong, G., Jin, Z., Painemal, D., Palikonda, R., Scarino, B. R., Spangenberg, D. A., Smith, R. A., Trepte, Q. Z., Yang, P., & Xie, Y. (2021). CERES MODIS Cloud Product Retrievals for Edition 4—Part I: Algorithm Changes. IEEE Transactions on Geoscience and Remote Sensing, 59(4), 2744-2780. https://doi.org/10.1109/tgrs.2020.3008866

Minnis, P., Sun-Mack, S., Young, D. F., Heck, P. W., Garber, D. P., Chen, Y., Spangenberg, D. A., Arduini, R. F., Trepte, Q. Z., Smith, W. L., Ayers, J. K., Gibson, S. C., Miller, W. F., Hong, G., Chakrapani, V., Takano, Y., Liou, K.-N., Xie, Y., & Yang, P. (2011). CERES Edition-2 Cloud Property Retrievals Using TRMM VIRS and Terra and Aqua MODIS Data—Part I: Algorithms. IEEE Transactions on Geoscience and Remote Sensing, 49(11), 4374-4400. https://doi.org/10.1109/tgrs.2011.2144601

Morrison, H., Curry, J. A., and Khvorostyanov, V. I.: A New Double-Moment Microphysics Parameterization for Application in Cloud and Climate Models. Part I: Description, J. Atmos. Sci., 62, 1665–1677, https://doi.org/10.1175/JAS3446.1, 2005.

Morrison, H., & Gettelman, A. (2008). A new two-moment bulk stratiform cloud microphysics scheme in the Community Atmosphere Model, version 3 (CAM3). Part I: Description and numerical tests. Journal of Climate, 21(15), 3642–3659. https://doi.org/10.1175/2008JCLI2105.1

Morrison, H., Thompson, G., and Tatarskii, V.: Impact of Cloud Microphysics on the Development of Trailing Stratiform Precipitation in a Simulated Squall Line: Comparison of One- and Two-Moment Schemes, Monthly Weather Review, 137, 991-1007, https://doi.org/10.1175/2008MWR2556.1, 2009.

Mülmenst.dt, J., Gryspeerdt, E., Dipu, S., Quaas, J., Ackerman, A. S., Fridlind, A. M., et al. (2024). General circulation models simulate negative liquid water path–droplet number correlations, but anthropogenic aerosols still increase simulated liquid water path. EGUsphere, 2024(12), 1–29. https://doi.org/10.5194/acp-24-7331-2024

Oue, M., Tatarevic, A., Kollias, P., Wang, D., Yu, K., & Vogelmann, A. M. (2020). The Cloud-resolving model Radar SIMulator (CR-SIM) Version 3.3: description and applications of a virtual observatory. *Geoscientific Model Development*, *13*(4), 1975-1998.

Painemal, D., Spangenberg, D., Smith Jr.,W. L., Minnis, P., Cairns, B., Moore, R. H., Crosbie, E., Robinson, C., Thornhill, K. L., Winstead, E. L., and Ziemba, L.: Evaluation of satellite retrievals of liquid clouds from the GOES-13 imager and MODIS over the midlatitude North Atlantic during the NAAMES campaign, Atmos. Meas. Tech., 14, 6633–6646, https://doi.org/10.5194/amt-14-6633-2021, 2021.

Platnick, S. (2000). Vertical photon transport in cloud remote sensing problems. *Journal of Geophysical Research: Atmospheres*, *105*(D18), 22919-22935.

Qiu, S., & Williams, I. N. (2020). Observational evidence of state-dependent positive and negative land surface feedback on afternoon deep convection over the Southern Great Plains. *Geophysical Research Letters*, *47*(5), e2019GL086622.

Qiu, S., Zheng, X., Painemal, D., Terai, C. R., and Zhou, X.: Daytime variation in the aerosol indirect effect for warm marine boundary layer clouds in the eastern North Atlantic, Atmos. Chem. Phys., 24, 2913-2935, 10.5194/acp-24-2913-2024, 2024.

Rémillard, J., Kollias, P., Luke, E., and Wood, R.: Marine Boundary Layer Cloud Observations in the Azores, J. Climate, 25, 7381–7398, https://doi.org/10.1175/JCLI-D-11-00610.1, 2012.

Sato, Y., Goto, D., Michibata, T., Suzuki, K., Takemura, T., Tomita, H., and Nakajima, T.: Aerosol effects on cloud water amounts were successfully simulated by a global cloud-system resolving model, Nat. Commun., 9, 985, https://doi.org/10.1038/s41467-018-03379-6, 2018.

Seifert, A., T. Heus, R. Pincus, and B. Stevens (2015), Large-eddy simulation of the transient and nearequilibrium behavior of precipitating shallow convection, J. Adv. Model. Earth Syst., 7, 1918–1937, doi:10.1002/2015MS000489.

Skamarock, W., Klemp, J., Dudhia, J., Gill, D., Liu, Z., Berner, J., and Huang, X.: A description of the advanced research WRF model version 4.3 (No. NCAR/TN-556+ STR).[Software], 2021.

Slingo, A. (1990). Sensitivity of the Earth's radiation budget to changes in low clouds. Nature, 343(6253), 49-51.

Small, J., Chuang, P., Feingold, G. & Jiang, H.: Can aerosol decrease cloud lifetime? Geophys. Res. Lett. 36, L16806, 2009.

Stephens, G. L., L'Ecuyer, T., Forbes, R., Gettelmen, A., Golaz, J. C., Bodas-Salcedo, A., ... & Haynes, J. (2010). Dreary state of precipitation in global models. Journal of Geophysical Research: Atmospheres, 115(D24).

Stevens, B., Cotton, W. R., Feingold, G., & Moeng, C. H. (1998). Large-eddy simulations of strongly precipitating, shallow, stratocumulus-topped boundary layers. Journal of the atmospheric sciences, 55(24), 3616-3638.

Stevens,B.,Satoh,M.,Auger,L.,Biercamp,J.,Bretherton,C.S.,Chen,X.,etal.(2019).DYAMOND:The Dynamics of the atmospheric general circulation modeled on non-hydrostatic domains. Progress in Earth and Planetary Science, 6(1), 61. https://doi.org/10.1186/s40645-019-0304-z.

Sun, Y., Solomon, S., Dai, A., & Portmann, R. W. (2006). How often does it rain?. Journal of climate, 19(6), 916-934.

Sun-Mack, S., Minnis, P., Chen, Y., Kato, S., Yi, Y., Gibson, S. C., et al.: Regional apparent boundary layer lapse rates determined from CALIPSO and MODIS data for cloud-height determination. Journal of Applied Meteorology and Climatology, 53(4), 990–1011, 2014.

Suzuki K, Nakajima TY, Stephens GL (2010). Particle growth and drop collection efficiency of warm clouds as inferred from Joint CloudSat and MODIS Observations. J Atmos Sci.;67(9):3019–32. https://doi.org/10.1175/2010JAS3463.1,

Suzuki, K., Stephens, G., Bodas-Salcedo, A., Wang, M., Golaz, J. C., Yokohata, T., & Koshiro, T. (2015). Evaluation of the warm rain formation process in global models with satellite observations. Journal of the Atmospheric Sciences, 72(10), 3996-4014.

Terai, C. R., Pritchard, M. S., Blossey, P., & Bretherton, C. S. (2020). The impact of resolving subkilometer processes on aerosol-cloud interactions of low-level clouds in global model simulations. Journal of Advances in Modeling Earth Systems,12, e2020MS002274. https://doi.org/10.1029/2020MS002274

Tian, J., Comstock, J., Geiss, A., Wu, P., Silber, I., Zhang, D., Kooloth, P. and Feng, Y.C., 2025. Mesoscale cellular convection detection and classification using convolutional neural networks: Insights from long-term observations at ARM Eastern North Atlantic site. *Journal of Geophysical Research: Machine Learning and Computation*, *2*(1), p.e2024JH000486.

Toll, V., Christensen, M., Quaas, J., and Bellouin, N.: Weak average liquid-cloud-water response to anthropogenic aerosols, Nature, 572, 51–55, https://doi.org/10.1038/s41586-019-1423-9, 2019.

Trepte, Q. Z., and Coauthors: Global cloud detection for CERES edition 4 using Terra and Aqua MODIS data. IEEE Trans. Geosci. Remote Sens., 57, 9410–9449, https://doi.org/10.1109/TGRS.2019.2926620, 2019.

Wang, Y., Zheng, X., Dong, X., Xi, B.,Wu, P., Logan, T., and Yung, Y. L.: Impacts of long-range transport of aerosols on marineboundary-layer clouds in the eastern North Atlantic, Atmos. Chem. Phys., 20, 14741–14755, https://doi.org/10.5194/acp-20-14741-2020, 2020.

Wang, Y., Zheng, G., Jensen, M., Knopf, D., Laskin, A., Matthews, A., ... & Wang, J. (2021). Vertical profiles of trace gas and aerosol properties over the eastern North Atlantic: variations with season and synoptic condition. *Atmospheric Chemistry and Physics Discussions*, *2021*, 1-39.

Wood, R., Wyant, M., Bretherton, C. S., Rémillard, J., Kollias, P., Fletcher, J., ... & Lin, Y. (2015). Clouds, aerosols, and precipitation in the marine boundary layer: An arm mobile facility deployment. *Bulletin of the American Meteorological Society*, *96*(3), 419-440.

Wu, P., Dong, X., & Xi, B. (2020). A climatology of marine boundary layer cloud and drizzle properties derived from ground-based observations over the Azores. *Journal of Climate*, *33*(23), 10133-10148.

Xue, H., & Feingold, G. (2006). Large-eddy simulations of trade wind cumuli: Investigation of aerosol indirect effects. Journal of the atmospheric sciences, 63(6), 1605-1622.

Xue H, Feingold G, Stevens B. Aerosol effects on clouds, precipitation, and the organization of shallow cumulus convection. J Atmos Sci. 2008;65(2):392–406. https://doi.org/10.1175/2007JAS2428.1.

Yuan, T. et al. Observational evidence of strong forcing from aerosol effect on low cloud coverage. Sci. Adv. 9, eadh7716 (2023).

Yuan, T., Song, H., Oreopoulos, L., Wood, R., Bian, H., Breen, K., Chin, M., Yu, H., Barahona, D., Meyer, K. and Platnick, S., 2024. Abrupt reduction in shipping emission as an inadvertent geoengineering termination shock produces substantial radiative warming. *Communications Earth & Environment*, *5*(1), p.281.

Zhang, Z., Song, Q., Mechem, D., Larson, V., Wang, J., Liu, Y., ... & Wu, P. (2020). Vertical Dependence of Horizontal Variation of Cloud Microphysics: Observations from the ACE-ENA field campaign and implications for warm rain simulation in climate models. *Atmospheric Chemistry and Physics Discussions*, *2020*, 1-46.

Zhang, J., Zhou, X., Goren, T., and Feingold, G.: Albedo susceptibility of northeastern Pacific stratocumulus: the role of covarying meteorological conditions, Atmos. Chem. Phys., 22, 861–880, https://doi.org/10.5194/acp-22-861-2022, 2022.

Zhang, J., and Feingold, G.: Distinct regional meteorological influences on low-cloud albedo susceptibility over global marine stratocumulus regions, Atmos. Chem. Phys., 23, 1073–1090, https://doi.org/10.5194/acp-23-1073-2023, 2023.

Zhang, J., Chen, Y.-S., Yamaguchi, T., and Feingold, G.: Cloud water adjustments to aerosol perturbations are buffered by solar heating in non-precipitating marine stratocumuli, Atmos. Chem. Phys., 24, 10425–10440, https://doi.org/10.5194/acp-24-10425-2024, 2024.

Zheng, X., Albrecht, B. A., H. H. Jonsson, D. Khelif, G. Feingold, P. Minnis, K. Ayers, P. Chuang, S. Donaher, D. Rossiter, V. Ghate, J. Ruiz-Plancarte, and S. Sun-Mack, 2011: Observations of the boundary layer, cloud, and aerosol variability in the southeast Pacific near-coastal marine stratocumulus during VOCALS-REx. *Atmos. Chem. Phys.*, 11, 9943-9959, doi: 10.5194/acp-11-9943-2011.

Zheng, X., Qiu, S., Zhang, D., Adebiyi, A., Zheng, X., Faruque, O., et al. (2025). Variability of eastern north Atlantic summertime marine boundary layer clouds and aerosols across different synoptic regimes identified with multiple conditions. Journal of Geophysical Research: Atmospheres, 130, e2024JD042240. https://doi.org/10.1029/ 2024JD042240

Zheng, X., Dong, X., Xi, B., Logan, T., & Wang, Y. (2024). Distinctive aerosol–cloud–precipitation interactions in marine boundary layer clouds from the ACE-ENA and SOCRATES aircraft field campaigns. *Atmospheric Chemistry and Physics*, *24*(18), 10323-10347.

Zhou, X., & Feingold, G. (2023). Impacts of mesoscale cloud organization on aerosol-induced cloud water adjustment and cloud brightness. Geophysical Research Letters, 50(13), e2023GL103417. https://doi.org/10.1029/2023gl103417

Zhou, X., Painemal, D., Gettleman, A., & Feingold, G. (2025). Exploring causal relationships and adjustment timescales of aerosol-cloud interactions in geostationary satellite observations and CAM6 using wavelet phase coherence analysis. Geophysical Research Letters, 52, e2024GL111961. https://doi.org/10.1029/2024GL111961